Article

Immunity

Environmentally induced cell stiffening shapes metastatic site selection by tuning the immune vulnerability of cancer cells

Graphical abstract

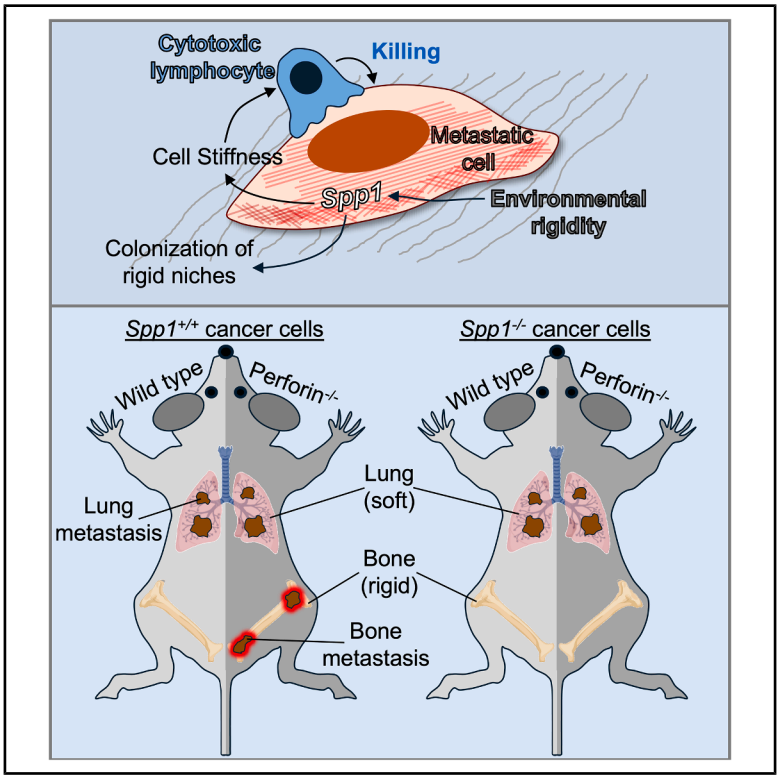

Authors

Yassmin A. Elbanna, Maria Tello-Lafoz, Aliya Holland, ..., Ori Barzilai, Scott R. Manalis, Morgan Huse

Correspondence

husem@mskcc.org

In brief

Adherent cells mimic the mechanical properties of their surroundings, becoming stiffer in more rigid environments and softer in more compliant ones. Elbanna et al. find that this environmentally induced stiffening response shapes metastatic site distribution by preferentially sensitizing cancer cells to cytotoxic lymphocytes in stiff contexts, such as the bone.

Highlights

- Metastatic cells stiffen in response to the rigidity of their microenvironment
- Cytotoxic lymphocytes disproportionately restrain metastasis in the rigid bone
- *Spp1* controls the mechanical adaptation and immune vulnerability of metastatic cells
- Tumor cell stiffness associates with environment rigidity and immune exclusion in humans

Elbanna et al., 2026, Immunity *59*, 1–17
August 11, 2026
https://doi.org/10.1016/j.immuni.2026.06.025

CellPress

Immunity

CellPress
OPEN ACCESS

Article

Environmentally induced cell stiffening shapes metastatic site selection by tuning the immune vulnerability of cancer cells

Yassmin A. Elbanna,[1] Maria Tello-Lafoz,[2,11] Aliya Holland,[3,11] Ye Zhang,[4,11] Chengyuan Li,[5] Seema Amin,[6] Zhenghan Wang,[7] Jun-Goo Kwak,[6] Alexandrina Yakimov,[2] Anastasiia Vaska,[2] Esther Lee,[2] Myra Dada,[4] Samuel Vayner,[4] Sarah M. Duquette,[4] Young Hun Kim,[8] Jahkwaun Budhai,[8] Ning Fan,[8] Erik Ladewig,[5] Tejus A. Bale,[9] Benjamin Y. Winer,[2] Kenny K.H. Yu,[10] Joan Massagué,[7] Christina Leslie,[5] Jungwoo Lee,[6] Ori Barzilai,[10] Scott R. Manalis,[4] and Morgan Huse[2,12,*]

[1]Louis V. Gerstner, Jr., Graduate School of Biomedical Sciences, Memorial Sloan Kettering Cancer Center, New York, NY, USA
[2]Immunology Program, Memorial Sloan Kettering Cancer Center, New York, NY, USA
[3]Pharmacology Program, Weill Cornell Graduate School of Medical Sciences, New York, NY, USA
[4]Koch Institute for Integrative Cancer Research and Department of Biological Engineering, Massachusetts Institute of Technology, Cambridge, MA, USA
[5]Computational Biology Program, Memorial Sloan Kettering Cancer Center, New York, NY, USA
[6]Department of Chemical Engineering, Institute for Applied Life Sciences, University of Massachusetts, Amherst, MA, USA
[7]Cancer Biology and Genetics Program, Memorial Sloan Kettering Cancer Center, New York, NY, USA
[8]Molecular Cytology Core Facility, Memorial Sloan Kettering Cancer Center, New York, NY, USA
[9]Department of Pathology and Laboratory Medicine, Memorial Sloan Kettering Cancer Center, New York, NY, USA
[10]Department of Neurosurgery, Memorial Sloan Kettering Cancer Center, New York, NY, USA
[11]These authors contributed equally
[12]Lead contact
*Correspondence: husem@mskcc.org
https://doi.org/10.1016/j.immuni.2026.06.025

SUMMARY

Metastatic microenvironments vary widely not only in their biochemical composition but also in their mechanical properties. Here, we examined how the mechanical rigidity of the metastatic niche affects metastases seeding and the local efficacy of antitumor immunosurveillance. Cancer cells stiffened in response to increasing environmental rigidity, a biophysical change that mechanically sensitized them to killing by cytotoxic lymphocytes. In immunodeficient mice, rigidity sensing by cancer cells yielded robust bone colonization, accompanied by marked stiffening of the cancer cells themselves. Conversely, in immunocompetent hosts, stiffer cancer cells were selectively eliminated, and bone metastasis was suppressed. In patients, metastatic cell stiffness was associated directly with environmental rigidity and inversely with immune infiltration. Expression of *Spp1*, encoding the secreted glycoprotein osteopontin, defined a subset of cancer cells that expanded in the bone, and deletion of *Spp1* limited environmentally induced cancer cell stiffening, bone colonization, and immune vulnerability. Thus, environmental mechanosensing regulates both metastases seeding and antitumor immunity, providing an immunological basis for metastatic site selection.

INTRODUCTION

Metastasis accounts for the majority of cancer-related deaths,[1] highlighting the urgent need to understand the mechanisms of metastatic progression. A defining feature of metastasis is its positional diversity, with each disease colonizing target organs that vary widely in molecular composition, tissue architecture, and immune profile.[2–5] Much is now known about the cellular and biochemical features of metastatic niches and how they influence cancer cell colonization. By contrast, the interplay between the mechanical properties of these microenvironments and the cancer cells within them remains poorly understood. Rigidity, defined as resistance to mechanical deformation, is particularly variable between metastatic niches, with organs like the lung and brain being very soft and mineralized bone approaching the stiffness of steel.[6]

Adherent cell types, including many cancer cells, engage in continuous biomechanical crosstalk with their environment.[7–10] This process, termed mechanoreciprocity, is initiated by cytoskeletally derived force exertion against the extracellular matrix (ECM) and other cells in the surrounding milieu. This facilitates the activation of integrins and other mechanosensitive receptors, which transduce signals that influence the morphology, proliferation, polarity, and gene expression of the responding

Please cite this article in press as: Elbanna et al., Environmentally induced cell stiffening shapes metastatic site selection by tuning the immune vulnerability of cancer cells, Immunity (2026), https://doi.org/10.1016/j.immuni.2026.06.025

cell. An important consequence of mechanoreciprocity is that the responding cell mimics the physical properties of its surroundings, becoming stiffer in more rigid environments and softer in more pliable ones.[11–14] One would therefore expect that metastatic tumor cells (MTCs) occupying rigid niches would be stiffer than those in softer tissues. The implications of this mechanical equilibration for the invasiveness and immune vulnerability of MTCs are not known.

Metastatic progression is antagonized by cytotoxic lymphocytes, comprising $CD8^+$ cytotoxic T lymphocytes (CTLs) and natural killer (NK) cells.[15,16] CTLs attack transformed target cells expressing neoantigens,[17] while NK cells attack targets that exhibit indices of stress or immune recognition.[18] Target cell engagement initiates the formation of a stereotyped cell-cell interaction, known as the immune synapse, into which the cytotoxic lymphocyte secretes toxic granzyme proteases and the pore-forming protein perforin to elicit programmed cell death.[19] The importance of this pathway for antitumor immunity is underscored by the clinical success of immunotherapeutic treatments that function by boosting cytotoxic lymphocyte activity.[20]

Immune synapses respond not only to the biochemical composition of the target cell but also to its mechanical properties.[21] This mechanosensitive behavior is thought to arise from the activating immunoreceptors responsible for synapse formation. A number of these proteins, including the T cell antigen receptor (TCR), certain activating NK receptors, and integrins like LFA-1 (lymphocyte function-associated antigen-1, $\alpha_L\beta_2$), only achieve optimal ligand binding and signaling when placed under tension.[22–24] This requirement imposes physical demands on the target cell, which must be rigid enough to counterbalance the load placed on mechanosensitive receptors and their ligands. Hence, stiffer surfaces bearing stimulatory ligands induce stronger lymphocyte activation than softer surfaces coated with the same proteins.[25–28] Importantly, this type of mechanosensing drives the preferential destruction of stiffer cancer cells by cytotoxic lymphocytes,[29–31] a process we call mechanosurveillance.

In this study, we explored the implications of mechanosurveillance and mechanoreciprocity for metastatic progression in biophysically disparate organs. Using murine models of metastasis and human patient samples, we found that cancer cells colonizing rigid *in vivo* environments stiffen mechanoreciprocally and that this sensitizes them to destruction by cytotoxic lymphocytes. We also identified the secreted ECM protein osteopontin as a critical mediator of environmentally induced cancer cell stiffening, metastatic invasion, and immune targeting. These results demonstrate how interplay between mechanoreciprocity and mechanosurveillance dictates not only the amount of metastatic burden but also the sites where outgrowth occurs.

RESULTS

Environmental rigidity controls the stiffness and immune recognition of cancer cells

To explore the effects of environmental rigidity on the mechanics of metastatic cells, we cultured B16F10 melanoma cells on substrates of varying rigidity, ranging from soft polyacrylamide hydrogels (8 kPa Young's modulus) to stiffer hydrogels (50 kPa) and tissue culture plastic (~1 GPa). After 24 h, cells were replated on glass and their stiffness measured by atomic force microscopy (AFM) (Figure 1A). We observed a progressive increase in cell stiffness that reflected the rigidity of the initial substrate (Figure 1B). These differences fell short of statistical significance, however, likely due to insufficient sample size. To address this issue, we turned to the suspended microchannel resonator (SMR), a microfluidic device in which suspension cells flow through a hairpin-shaped microchannel embedded in a vibrating cantilever (Figure 1C). The vibration creates a standing acoustic wave within the channel, and as cells flow through the node of the cantilever, they induce vibrational frequency shifts that depend on each cell's size-normalized acoustic scattering (SNACS), a parameter that increases monotonically with cell stiffness.[32] SMR is three orders of magnitude faster than traditional AFM, and because it does not require replating, it circumvents artifacts arising from adaptation to a second substrate. Our SMR measurements mirrored our AFM results but with larger sample size, additional stiffness regimes, and enhanced statistical power (Figure 1D). We conclude that B16F10 cells exhibit mechanoreciprocity, becoming stiffer in more rigid environments.

Next, we examined the capacity of environmental stiffness to sensitize B16F10 targets to cytotoxic lymphocytes. B16F10 cells cultured on substrates of increasing rigidity were loaded with $ovalbumin_{257–264}$ peptide (OVA) and then mixed with CTLs expressing the OT-1 TCR, which recognizes OVA in the context of the major histocompatibility complex class I (MHC class I) H-$2K^b$ (Figure 1E). On stiffer substrates, B16F10 cells elicited markedly stronger CTL activation, which we measured by production of the cytokines IFNγ and TNF (Figure 1F). Increased substrate rigidity also enhanced B16F10 killing by both CTLs and NK cells (Figures 1E, 1G, and 1H). Hence, rigid environments render cancer cells more stimulatory to cytotoxic lymphocytes and more vulnerable to their killing responses.

Environmental rigidity sensitizes MTCs to cytotoxic lymphocytes *in vivo*

The capacity of substrate rigidity to dictate the stiffness and immune vulnerability of cancer cells *in vitro* prompted us to hypothesize that cancer cells invading stiff organs would be sensitized to immunosurveillance *in vivo*. To address this question, we intravenously (i.v.) injected Luciferase-expressing (Luc^+) B16F10 cells into immunocompetent C57BL/6 mice (wild type [WT]) or into perforin knockout ($Prf1^{-/-}$) mice, which lack the predominant pathway for cellular cytotoxicity (Figure 2A). Within 3 weeks, WT recipients exhibited frank metastases that were predominantly situated in the lungs (Figure 2B). $Prf1^{-/-}$ animals displayed a different outgrowth pattern; not only did metastases appear more quickly, but they also manifested in both the lungs and in the long bones of the leg (femurs) (Figure 2B). The emergence of bone metastasis was not simply the by-product of globally increased outgrowth, as injection of 8-fold more B16F10 cells into WT animals enhanced lung colonization without seeding detectable growth in the bone (Figure S1A). To quantify differential metastatic site distribution, we determined the fraction of total bioluminescence coming from the legs (Figures 2C and S1B), and we also compared the increase in femoral outgrowth observed in $Prf1^{-/-}$ recipients to the increase in total outgrowth (Figure 2D). Both approaches confirmed the selective expansion

Please cite this article in press as: Elbanna et al., Environmentally induced cell stiffening shapes metastatic site selection by tuning the immune vulnerability of cancer cells, Immunity (2026), https://doi.org/10.1016/j.immuni.2026.06.025

CellPress
OPEN ACCESS

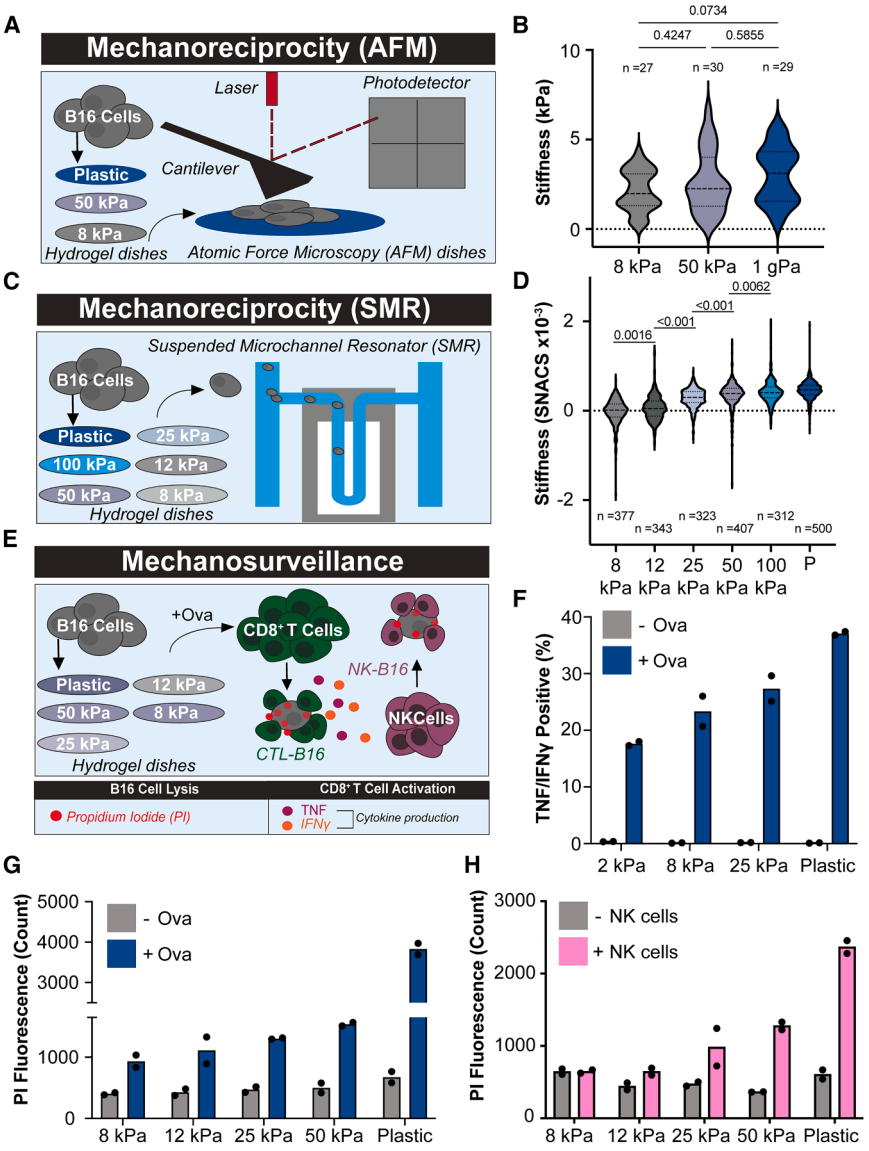

Figure 1. Substrate rigidity stiffens cancer cells and sensitizes them to cytotoxic lymphocytes

(A–D) B16F10 cells were cultured overnight on substrates of differential rigidity, and stiffness measurements of individual cells performed by AFM (A and B) or SMR (C and D). (A) and (C) show schematic diagrams of the approach.

(B and D) Cell stiffness measurements at the indicated substrate rigidities, determined by AFM (B) and SMR (D). Violins encompass the entire data distribution, with dashed lines denoting the median and dotted lines indicating the upper and lower quartiles. Samples sizes (n =) are displayed above (B) or below (D) each violin. p values calculated by one-way ANOVA.

(E–H) B16F10 cells cultured overnight on substrates of differential rigidity were mixed with NK cells or with OT-1 CTLs in the presence of OVA, followed by quantification of B16F10 killing and CTL cytokine production.

(E) Schematic diagram of the approach.

(F) CTL cytokine production, expressed as the percentage of $TNF^+IFN\gamma^+$ CTLs after 5 h coculture with B16F10 cells.

(G and H) B16F10 killing by CTLs (G) and NK cells (H), measured by propidium iodide uptake into dead cells after 5 h in the presence or absence of OVA (G) or the presence or absence of NK cells (H). All results are representative of at least two independent experiments.

of femoral metastasis in *Prf1*$^{-/-}$ mice. Enhanced colonization was also detected in other rigid locations, including the heart, skull, and spine (Figures 2F, S1C, and S1D). Histological analysis of femoral tumors highlighted the tendency of cancer cells to accumulate in the metaphyseal space, an area enriched in trabecular bone (Figure 2E). Within spinal tumors, cancer cells occupied the vertebral body and articular processes while also invading the epidural space (Figures 2F and S1D). This growth pattern would be expected to compress the spinal cord, and consistently, we found that most *Prf1*$^{-/-}$ mice, but not their WT counterparts, developed hind-leg paralysis after B16F10 injection (Figure 2G). Collectively, these results indicate that perforin-mediated killing is particularly important for suppressing bone metastasis.

Given that previous studies suggesting that perforin deficiency can drive generalized immune activation,[33–35] we also quantified myeloid cells in the lungs and bone marrow. WT and *Prf1*$^{-/-}$ mice had similar numbers of neutrophils, dendritic cells, and monocytes in each organ in both the presence and the absence of cancer cells (Figure S1E). A slight increase in M1 macrophages and a small (but statistically insignificant) decrease in M2 macrophages was observed in *Prf1*$^{-/-}$ bone marrow after B16F10 injection, likely reflecting the presence of bone metastases in tumor-bearing *Prf1*$^{-/-}$ mice and not in WT controls. Taken together with the results above, these data suggest that cytotoxic lymphocytes kill most MTCs directly in this system rather than secondarily via myeloid cell activation.

Immunofluorescence staining of B16F10 bone metastases revealed more pronounced accumulation of NK cells than $CD8^+$ T cells (Figure 2H), implying a more important role for the former in the surveillance of this cell line *in vivo*. Consistent with this interpretation, mice treated with an NK cell depleting antibody exhibited enhanced femoral colonization relative to mice receiving an isotype control antibody (Figures 3A–3C, S2A, and S2B). Furthermore, NK cell-depleted animals, but not isotype-injected controls, developed spine metastases and hind-leg paralysis after B16F10 injection (Figures 3D, 3E, and S2C). By contrast, depletion of $CD8^+$ T cells affected neither metastatic site distribution nor outgrowth (Figures S2D–S2F). We conclude that NK cells play the predominant role in limiting B16F10 bone metastasis in this model system.

Please cite this article in press as: Elbanna et al., Environmentally induced cell stiffening shapes metastatic site selection by tuning the immune vulnerability of cancer cells, Immunity (2026), https://doi.org/10.1016/j.immuni.2026.06.025

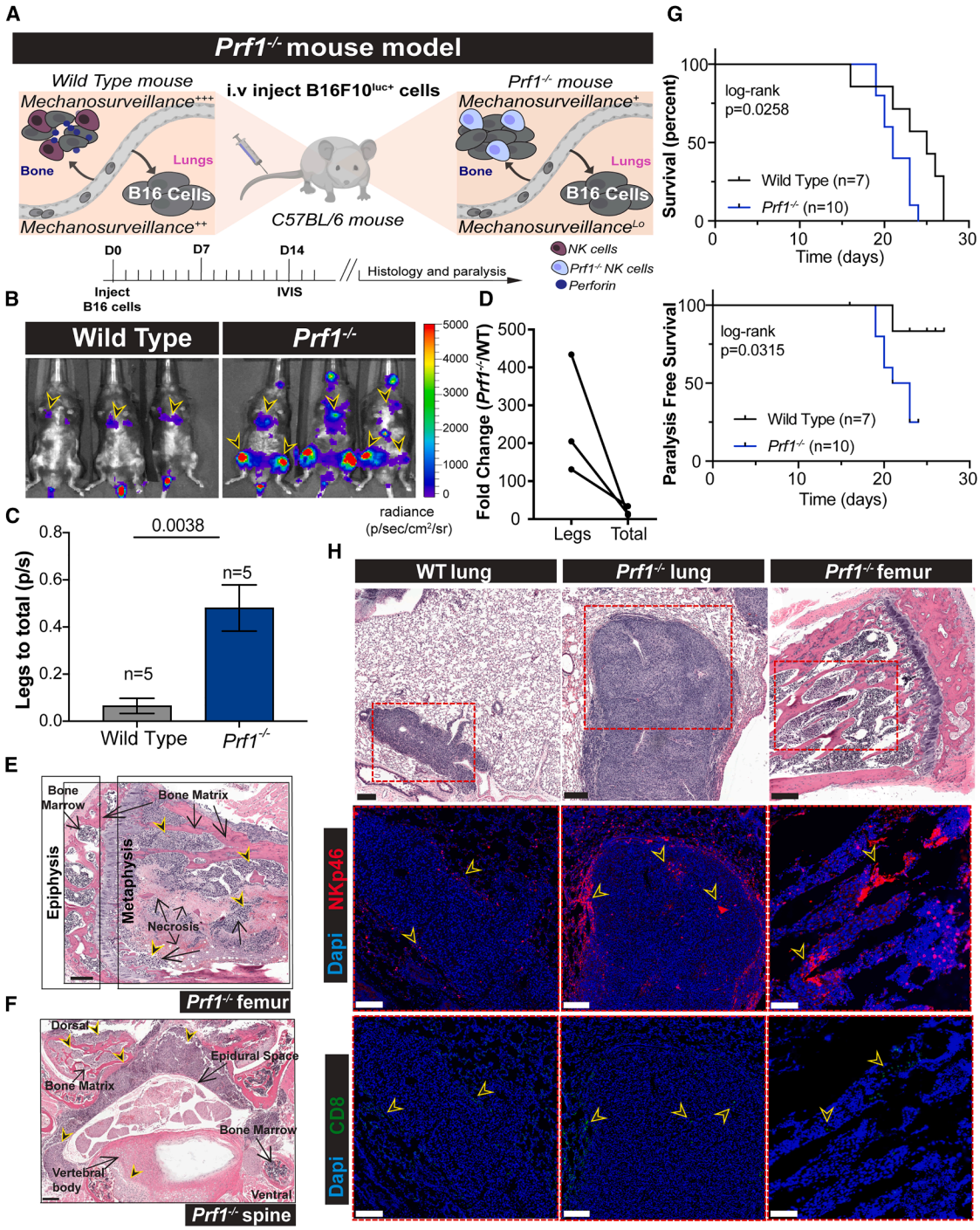

Figure 2. Preferential suppression of bone metastasis by cytotoxic lymphocytes

Luc^{+} B16F10 cells were injected i.v. into wild-type (WT) and *Prf1*$^{-/-}$ mice, which were then monitored for metastatic colonization.

(A) Schematic diagram of the experimental approach.

(B) Representative bioluminescence images of tumor-bearing WT and *Prf1*$^{-/-}$ mice, with metastatic burden in the lungs and femurs indicated by black and yellow arrowheads.

(C) Quantification of femoral colonization in a representative experiment, expressed as a ratio of bioluminescence signal in the legs to the total bioluminescence signal. Error bars denote standard error of the mean (SEM). Sample size is indicated above each bar. *p* value calculated by unpaired Student's *t* test.

(D) Mean fold change of B16F10 colonization in *Prf1*$^{-/-}$ mice relative to WT controls, determined for total metastasis and femoral metastasis (legs). Paired values were derived from 3 independent experiments.

(E and F) Representative H&E images of B16F10 bone metastases in the femur (E) and spine (F) of a *Prf1*$^{-/-}$ mouse. Epiphysis and metaphysis of the femur are indicated, with tumor cells denoted by black and yellow arrowheads. Scale bars, 200 μm.

(legend continued on next page)

Please cite this article in press as: Elbanna et al., Environmentally induced cell stiffening shapes metastatic site selection by tuning the immune vulnerability of cancer cells, Immunity (2026), https://doi.org/10.1016/j.immuni.2026.06.025

To extend our findings to another melanoma model, we turned to YUMM5.2 cells, which contain driver mutations (oncogenic $Braf^{V600E}$ and loss of P53) that are common in human disease. Because YUMM5.2 cells expand more slowly than B16F10 cells *in vivo*, we injected them via the intracardiac (i.c.) route, which enhances metastatic seeding in organs other than the lungs.[36] In WT recipients, YUMM5.2 cells predominantly formed abdominal metastases, with some mice exhibiting modest growth in the femur (Figure S2G). This femoral colonization increased disproportionately in $Prf1^{-/-}$ animals (Figures S2H and S2I), implying preferential cytotoxic lymphocyte targeting of bone metastasis. Notably, the magnitude of this increase was less pronounced than what we had observed with B16F10 cells, consistent with prior work indicating that YUMM5.2 tumors are only weakly immunogenic.[36] To investigate non-melanoma malignancies, we employed i.c. injection of MC38 colon cancer cells, which are used extensively to study antitumor immunity.[37] MC38 femoral tumor burden was markedly enhanced in $Prf1^{-/-}$ mice (Figures S2J–S2L), mirroring our results with B16F10 and YUMM5.2 cells. Hence, the preferential suppression of bone metastasis by cytotoxic lymphocytes applies to multiple types of cancer.

Next, we investigated whether increased environmental rigidity is sufficient to enhance antitumor responses, independently of other environmental differences. Our studies utilized an implantable microenvironment system recently developed to study colonization by disseminated cancer cells.[38] 6 mm × 1 mm hydrogel discs of differential rigidity (15 wt % versus 30 wt % polyacrylamide) were implanted subcutaneously in opposing flanks of C57BL/6 mice. Following a period of vascularization and engraftment, the animals were treated with NK cell depleting or isotype control antibodies. Luc^+ B16F10 cells were then i.v. injected and their relative colonization of soft and stiff hydrogel scaffolds evaluated after 3 weeks (Figures 3F and 3G). Preferential colonization of the stiffer hydrogels was observed in 8 out of 9 NK-depleted mice (Figure 3H), suggestive of an invasion or growth advantage in more rigid microenvironments. This predilection was notably absent in control mice (Figure 3H), implying that cancer cells occupying more rigid hydrogel niches are also more sensitive to NK cells. The observation that environmental rigidity can, on its own, enhance antitumor immunity *in vivo* provides a mechanobiological basis for the preferential targeting of bone metastasis by cytotoxic lymphocytes.

Immune pressure and the microenvironment dictate MTC stiffness in mice and humans

The hypothesis that mechanoreciprocity within the metastatic niche dictates the sensitivity of cancer cells to mechanosurveillance makes two *in vivo* predictions. The first of these, addressed above, is that cancer cells colonizing rigid microenvironments should be more vulnerable to cytotoxic lymphocytes. The second is that MTC stiffness should reflect both environmental rigidity and the level of cytotoxic immune pressure; MTCs colonizing rigid environments should be stiffer than cells from soft organs due to mechanoreciprocity, and MTCs from mice lacking cytotoxic lymphocyte activity should be stiffer than cells from immunocompetent animals due to mechanosurveillance.

To evaluate these hypotheses, we i.v. injected WT and $Prf1^{-/-}$ mice with GFP-expressing (GFP^+) B16F10 cells, then used SMR to profile MTC stiffness after FACS purification from the lungs and femurs of $Prf1^{-/-}$ recipients and from the lungs of WT recipients (WT mice rarely develop bone metastases after i.v. injection) (Figure 4A). Lung MTCs from $Prf1^{-/-}$ animals exhibited significantly higher stiffnesses than lung MTCs from WT animals (Figure 4B), in line with the expectation that stiffer cancer cells are preferentially destroyed by mechanosurveillance. Furthermore, MTCs from $Prf1^{-/-}$ femoral metastases were markedly stiffer than both lung samples (Figure 4B), indicative of mechanoreciprocity in the bone microenvironment. We observed a similar pattern of results in experiments comparing NK cell-depleted recipient mice with isotype antibody-treated controls. MTCs from NK-depleted lungs were stiffer than MTCs from isotype lungs, and MTCs from NK-depleted bone were stiffer than both lung samples (Figure 4C). Thus, MTCs from biophysically distinct organs exhibit mechanical phenotypes consistent with the effects of both mechanoreciprocity and mechanosurveillance.

To extend this line of investigation to human metastasis, we developed an approach based on analyzing physically contiguous spinal metastases spanning both the osseous (bony) regions of vertebrae as well as the soft epidural space around the spinal cord (Figure 4D). By resecting samples from the osseous and epidural components of the same patient metastasis, we were able to compare isogenic MTC preparations from two mechanically distinct environments. Samples from two patients with breast cancer and two patients with non-small cell lung cancer (NSCLC) were dissociated and FACS purified to isolate $EpCAM^+$ MTCs, which were then subjected to SMR. Osseous MTCs from the breast cancer samples were substantially stiffer than their epidural counterparts (Figure 4E), consistent with mechanoreciprocity in the bone microenvironment. Interestingly, this pattern was not observed in the NSCLC samples, where osseous MTCs were actually a bit softer than MTCs from the epidural space (Figure 4F). We reasoned that these discrepancies might reflect differential cytotoxic lymphocyte involvement during metastatic colonization. NSCLC is generally more immunogenic than breast cancer, reflecting a higher mutational load.[39,40] Augmented mechanosurveillance by cytotoxic lymphocytes would be expected to preferentially deplete stiffer MTCs in the bone, thereby reversing the effects of mechanoreciprocity in this tissue.

To investigate this possibility, the same patient samples were stained for CD45 (a pan-leukocyte marker), CD3 (for T cells), CD8 (for CTLs), and CD56 (for NK cells). NSCLC metastases were

(G) Survival and paralysis-free survival of tumor-bearing WT and $Prf1^{-/-}$ mice.
(H) H&E images of representative metastatic tumors from the indicated tissues are shown above and immunofluorescence staining of adjacent sections shown below, with $NKp46^+$ NK cells in red and $CD8^+$ T cells in green. Boxes in the H&E sections indicate the approximate scope of the immunofluorescence images. Black and yellow arrowheads denote NK cell clusters in the $Prf1^{-/-}$ tumors and isolated NK cells and $CD8^+$ T cells in the other images. Scale bars, 200 μm. All results are representative of at least two independent experiments.
See also Figure S1.

Please cite this article in press as: Elbanna et al., Environmentally induced cell stiffening shapes metastatic site selection by tuning the immune vulnerability of cancer cells, Immunity (2026), https://doi.org/10.1016/j.immuni.2026.06.025

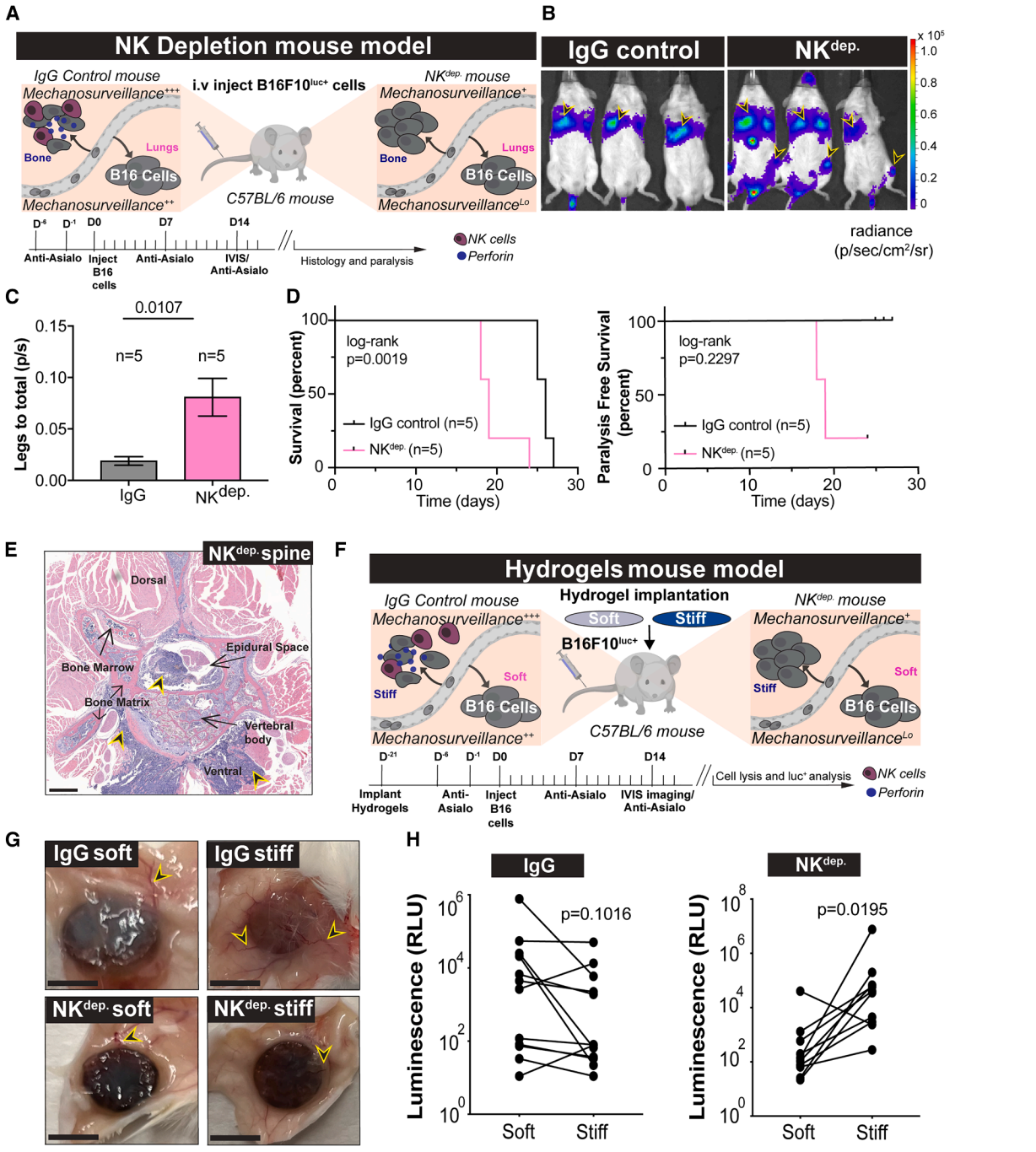

Figure 3. NK cells preferentially suppress metastasis in rigid environments

Luc$^+$ B16F10 cells were injected i.v. into IgG control and NK depleted (NK$^{dep.}$) mice, which were then monitored for metastatic colonization.

(A) Schematic diagram of the experimental approach.

(B) Representative bioluminescence images of tumor-bearing IgG control and NK$^{dep.}$ mice, with metastatic burden in the lungs and femurs indicated by black and yellow arrowheads.

(C) Quantification of femoral colonization in a representative experiment, expressed as a ratio of bioluminescence signal in the legs to the total bioluminescence signal. Error bars denote SEM. Sample size is indicated above each bar. *p* value calculated by unpaired Student's *t* test.

(D) Survival and paralysis-free survival of tumor-bearing control and NK$^{dep.}$ mice.

(E) Representative H&E image of B16F10 bone metastasis in the spine of an NK$^{dep.}$ mouse. Tumor cells indicated by black and yellow arrowheads. Scale bar, 500 μm.

(F–H) C57BL/6 mice bearing stiff and soft subcutaneous hydrogel implants were treated with IgG control or NK cell depleting antibodies and then i.v. injected with Luc$^+$ B16F10 cells. B16F10 colonization of the implants was assessed after 2 weeks.

(F) Schematic diagram of the experimental approach.

(legend continued on next page)

Please cite this article in press as: Elbanna et al., Environmentally induced cell stiffening shapes metastatic site selection by tuning the immune vulnerability of cancer cells, Immunity (2026), https://doi.org/10.1016/j.immuni.2026.06.025

characterized by marked lymphocytic infiltration. In NSCLC patient #1, this phenotype was driven by robust accumulation of $CD8^+$ CTLs, whereas in NSCLC patient #2, roughly equivalent numbers of $CD8^+$ and $CD56^+$ cells were detected in the tumor (Figures 4F and S3A). By contrast, the breast cancer metastases exhibited appreciably lower levels of CTLs and NK cells. Few lymphocytes were present in breast cancer tumor #1, and although breast cancer tumor #2 contained $CD8^+$ cells, almost all of them were segregated in interstitial regions between tumor subdomains (Figure 4E). Interestingly, these interstitial domains contained clusters of large, $CD45^+$ cells (Figure S3B), not unlike the macrophage-based lymphocyte exclusion barriers observed in certain metastatic tumors.[41–43] We conclude that observed MTC stiffness likely reflects the convolution of mechanoreciprocal stiffening and mechanosurveillance; under conditions of low cytotoxic lymphocyte infiltration (breast cancer), stiffened cells persist and expand, whereas when cytotoxic lymphocyte activity is high (NSCLC), stiffened cells are destroyed and the effects of mechanoreciprocity are suppressed.

Spp1 expression defines a subset of bone colonizing MTCs

To explore the mechanisms underlying stiffness modulation *in vivo*, GFP^+ B16F10 MTCs from the lungs of WT mice and from the lungs and bones of *Prf1*$^{-/-}$ mice were subjected to single cell RNA-sequencing (scRNA-seq). Uniform manifold approximation and projection (UMAP) analysis of the resulting data revealed nine populations of cancer cells (Figure 5A). Lung metastases from WT and *Prf1*$^{-/-}$ animals contained all 9 populations, implying that cellular cytotoxicity does not drastically alter the distribution of cancer cells in this organ. By contrast, B16F10 composition differed dramatically in *Prf1*$^{-/-}$ bone, with several clusters shifting substantially or disappearing altogether. Most striking was the enrichment of cluster 7, encompassing ~25% of cancer cells in *Prf1*$^{-/-}$ bone and only ~2% of the lung samples (Figure S4A).

Using differential gene expression analysis, we identified a suite of genes preferentially expressed in cluster 7 (Figure S4B). Among these was *Spp1*, which encodes osteopontin, a secreted ECM glycoprotein that is recognized by several cell surface receptors, including CD44 and the $\alpha_v\beta_3$ integrin.[45] Osteopontin was intriguing to us because it is highly expressed by bone-resident cells and because it promotes osteoclast adhesion to bone matrix.[46,47] Furthermore, certain transformed cell types induce osteopontin in response to substrate stiffness[48,49] and following entry into the bone microenvironment.[50] Consistent with these prior data, B16F10 cells produced more osteopontin when cultured on higher rigidity hydrogels (Figure S4C). In mouse models, osteopontin potentiates osteotropic metastases through cancer cell adhesion and migration,[51–54] while in human patients, high *SPP1* expression is a feature of bone metastasis and an indicator of its prevalence.[55–59] Using the Cancer Genome Atlas (TCGA), we found that *SPP1* amplification events were disproportionately represented in tumors from more rigid tissues (e.g., sarcoma), whereas *SPP1* deletion was more prominent in cancers originating in softer organs (e.g., glioblastoma) (Figure S4D). These observations suggest a role for osteopontin in adapting to rigid environments, and in line with this hypothesis, we found that cluster 7 B16F10 cells from the bone expressed higher levels of *Spp1* than did cluster 7 cells in either lung sample (Figure 5B). Similarly, bone-derived MTCs from NK-depleted mice expressed significantly more *Spp1* than did MTCs from the lungs of isotype control or NK-depleted animals (Figure S4E). Taken together, these results document the selective expansion of a subset of B16F10 cells during bone metastasis and identify osteopontin as an index of bone colonization.

Spp1 controls cancer cell stiffness and mechanosurveillance

The increased expression of *Spp1* by bone MTCs prompted us to interrogate its role as a mechanoregulator of metastatic site selection. Using CRISPR-Cas9, we generated two *Spp1*$^{-/-}$ B16F10 cell lines (Figures S5A and S5B), along with a control cell line prepared with nontargeting rather than *Spp1*-specific guide (g)RNA. *Spp1*$^{-/-}$ and *Spp1*$^{+/+}$ cells grew comparably *in vitro* (Figure S5C), indicating that osteopontin is dispensable for B16F10 proliferation. Both *Spp1*$^{-/-}$ cell lines, however, were significantly less stiff than *Spp1*$^{+/+}$ controls (Figures 5C and S5D), and they also contained significantly less F-actin (Figures S5E and S5F), which was indicative of enhanced deformability and also suggestive of feedback between osteopontin production and cytoskeletal strength. Notably, adding purified osteopontin protein restored the stiffness of *Spp1*$^{-/-}$ cells to WT levels (Figure S5G). Furthermore, we found that an additional, "safe-harbor" cell line, prepared by CRISPR-Cas9 targeting of the Rosa26 locus, retained WT stiffness (Figure S5H). Hence, the mechanical softening of *Spp1*$^{-/-}$ cells results specifically from loss of osteopontin rather than CRISPR-induced DNA damage. *Spp1*$^{-/-}$ cells were less susceptible than controls to CTL-mediated killing *in vitro* (Figure S6A), suggesting that osteopontin-dependent stiffening makes B16F10 cells more stimulatory to cytotoxic lymphocytes. In line with this interpretation, CTLs cocultured with *Spp1*$^{-/-}$ cells produced less IFNγ and TNF (Figure S6B). CTL release of cytotoxic proteins, which we measured by exposure of the secretory lysosome marker Lamp1, was also impaired (Figure S6C). Notably, *Spp1*$^{-/-}$ cells expressed normal levels of MHC class I, indicating that their diminished stimulatory capacity was not caused by reduced activating ligand expression (Figure S6D).

Collectively, these results strongly suggest that osteopontin increases the stiffness of cancer cells, thereby making them more vulnerable to mechanosurveillance. Accordingly, we reasoned that cells expressing more osteopontin would be preferentially depleted, or immunoedited, by cytotoxic lymphocytes *in vivo*. In line with this prediction, B16F10 MTCs from *Prf1*$^{-/-}$ lungs had higher *Spp1* levels than lung MTCs from WT mice (Figure 5B). Similarly, MC38 MTCs from *Prf1*$^{-/-}$ bones expressed more *Spp1* than MTCs from control bones (Figure S6E). To further

(G) Representative images of hydrogel implants 3 weeks after implantation, with black and yellow arrowheads denoting vascularization. Scale bars, 2.5 mm.
(H) Implant colonization by B16F10 cells in IgG control (left) and $NK^{dep.}$ (right) mice, measured by luciferase luminescence after hydrogel lysis. *p* value calculated by paired Mann-Whitney test. All results are representative of at least two independent experiments.
See also Figure S2.

Please cite this article in press as: Elbanna et al., Environmentally induced cell stiffening shapes metastatic site selection by tuning the immune vulnerability of cancer cells, Immunity (2026), https://doi.org/10.1016/j.immuni.2026.06.025

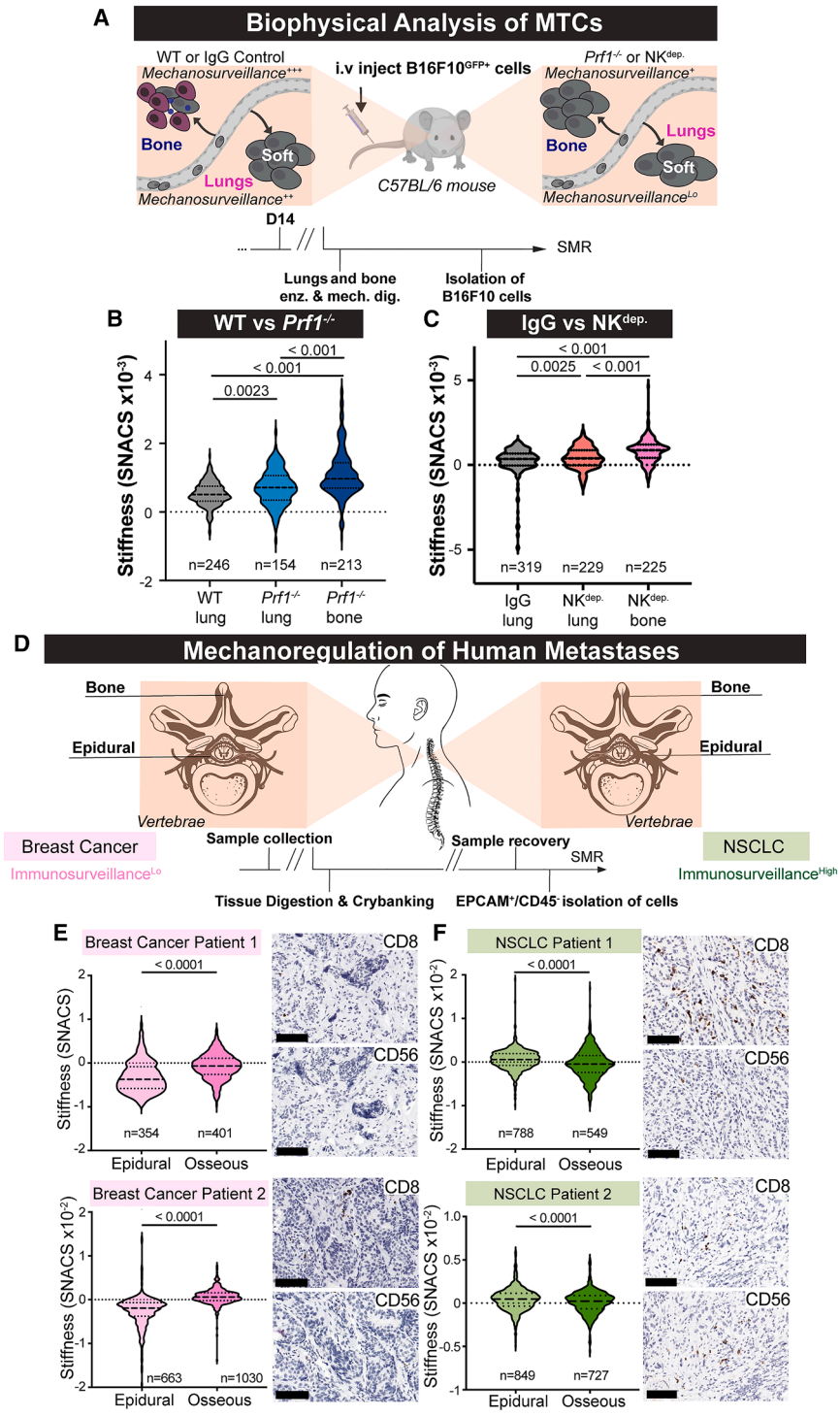

Figure 4. Environmental and immune regulation of MTC stiffness

GFP+ B16F10 cells were i.v. injected either into WT and *Prf1*$^{-/-}$ mice or into IgG control-treated and NK cell-depleted (NK$^{dep.}$) mice. After 2 weeks, MTCs from the resulting metastases in the lungs of WT or IgG control mice and the lungs and bones of *Prf1*$^{-/-}$ or NK$^{dep.}$ mice were extracted and subjected to SMR.

(A) Schematic diagram of the experimental approach.

(B and C) SMR of B16F10 MTCs isolated from the indicated organs of WT and *Prf1*$^{-/-}$ mice (B) or from IgG control and NK$^{dep.}$ mice (C). Violins encompass the entire data distribution, with dashed lines denoting the median and dotted lines indicating the upper and lower quartiles. Samples sizes (n =) are displayed below each violin. p values calculated by one-way ANOVA.

(D–F) Comparative analysis of MTCs from the osseous and epidural regions of human spinal metastases. (D) Schematic diagram illustrating anticipated differences in the immunosurveillance of breast cancer versus NSCLC metastases.

(E and F) Left, SMR of epidural and osseous spinal MTCs isolated from patients with metastatic breast cancer (E) or NSCLC (F). Right, representative IHC images showing CD8 and CD56 staining in epidural breast cancer (E) or NSCLC (F) sections. Scale bars, 100 μm.

In (E) and (F), violins encompass the entire data distribution, with dashed lines denoting the median and dotted lines indicating the upper and lower quartiles. Samples sizes (n =) are displayed below each violin. p values calculated by unpaired Student's t test.

See also Figure S3.

characterize this immunoediting effect, we mechanically profiled GFP+ *Spp1*$^{-/-}$ and *Spp1*$^{+/+}$ B16F10 MTCs from the lungs of WT and *Prf1*$^{-/-}$ mice (Figure 5D). Consistent with our initial *in vivo* SMR analysis (Figure 4B), *Spp1*$^{+/+}$ MTCs from *Prf1*$^{-/-}$ lungs were significantly stiffer than *Spp1*$^{+/+}$ MTCs from WT lungs (Figure 5E), indicating that stiffer MTCs in this organ are preferentially destroyed by cytotoxic lymphocytes. By contrast, *Spp1*$^{-/-}$ MTCs exhibited identical stiffness profiles regardless of whether they were purified from WT or *Prf1*$^{-/-}$ lungs (Figure 5E). Hence, to the extent that *Spp1*$^{-/-}$ cells experience immune selection *in vivo*, this selection is not based on stiffness.

To explore the relationship between *SPP1*, cancer cell mechanics, and mechanosurveillance in human disease, we examined publicly available transcriptomic datasets profiling human melanoma. Our efforts focused on a large scRNA-seq study of metastatic lesions from 23 patients with stage II/III disease.[44] All lesions were assessed histopathologically for infiltrating lymphocytes and classified as "absent," describing a tumor devoid of lymphocytes, "non-brisk," describing a tumor with some lymphocyte infiltration and some excluded areas, and "brisk," describing a highly infiltrated tumor. This classification enabled us to infer the specific impact of immune infiltration on cancer cell transcription (Figure 5F). In our initial UMAP analysis, cancer cells clustered predominantly by patient (Figures 5G and S6F), which was not unexpected, as underlying patient genetics was probably the predominant source of variation in this study.

Please cite this article in press as: Elbanna et al., Environmentally induced cell stiffening shapes metastatic site selection by tuning the immune vulnerability of cancer cells, Immunity (2026), https://doi.org/10.1016/j.immunni.2026.06.025

CellPress
OPEN ACCESS

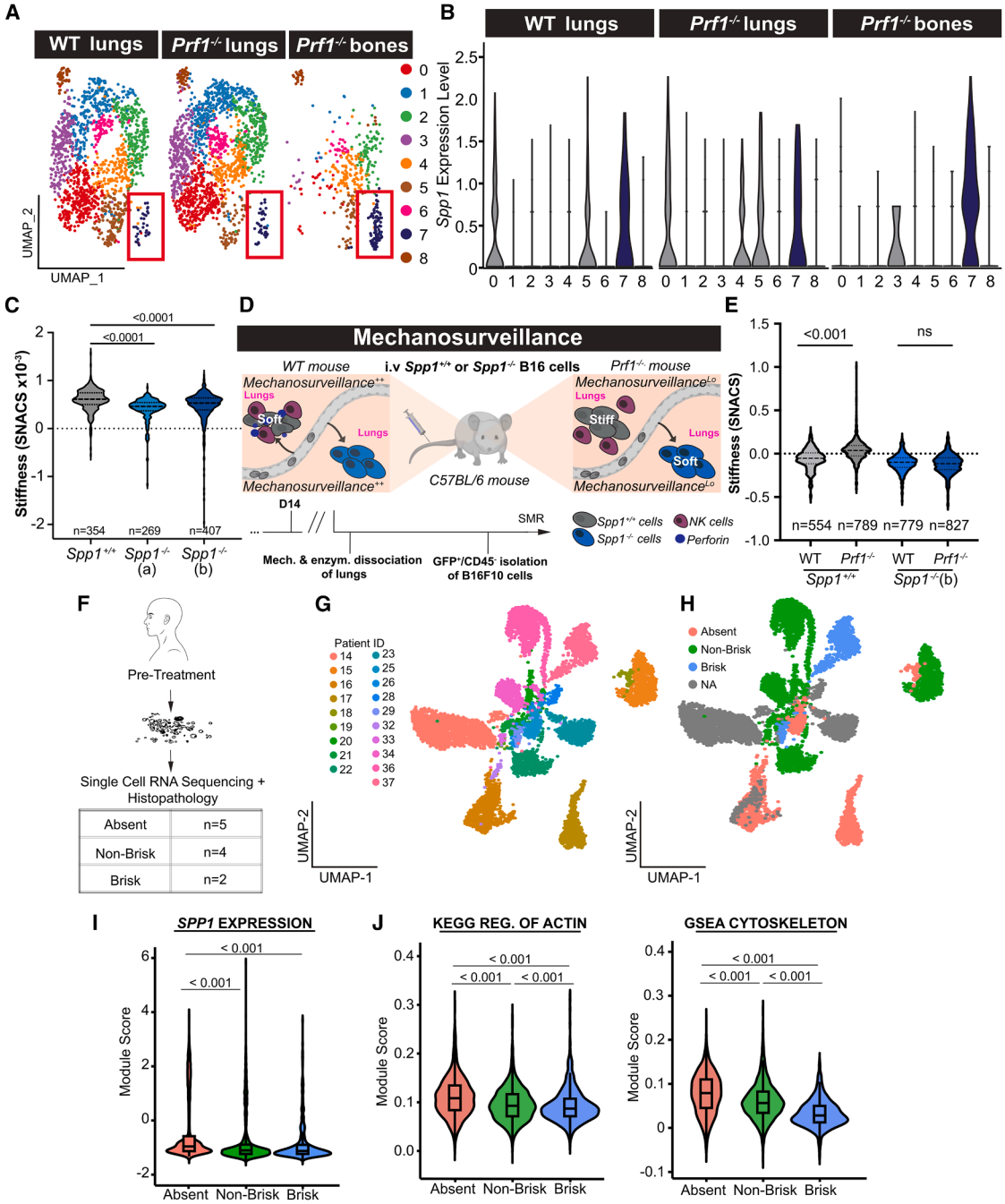

Figure 5. *Spp1* promotes mechanosurveillance in mice and humans

(A and B) GFP$^+$ B16F10 cells were i.v. injected into WT and *Prf1*$^{-/-}$ mice. After 2 weeks, MTCs from metastases in the lungs of WT mice and the lungs and bones of *Prf1*$^{-/-}$ mice were extracted and subjected to scRNA-seq.

(A) UMAP visualization of scRNA-seq data from the indicated lung and bone MTCs, clustered based on transcriptional similarity and colored by Seurat cluster identity. Cluster 7 is boxed in each graph.

(B) Violin plots showing *Spp1* expression levels across Seurat clusters in the indicated lung and bone metastases. Violins represent the distribution of *Spp1* expression within a cluster, with width indicating more cells.

(C) SMR of the indicated *Spp1*$^{+/+}$ and *Spp1*$^{-/-}$ B16F10 cell lines.

(D and E) GFP$^+$ *Spp1*$^{+/+}$ or *Spp1*$^{-/-}$ B16F10 cells were injected i.v. into WT and *Prf1*$^{-/-}$ mice, and after 2 weeks, MTCs from lung metastases were extracted and subjected to SMR.

(D) Schematic diagram of the experimental approach.

(legend continued on next page)

Please cite this article in press as: Elbanna et al., Environmentally induced cell stiffening shapes metastatic site selection by tuning the immune vulnerability of cancer cells, Immunity (2026), https://doi.org/10.1016/j.immuni.2026.06.025

We then evaluated the expression of cytoskeletal genes and *SPP1* as a function of lymphocyte infiltration. This analysis revealed increased expression of *SPP1* and of gene sets encompassing the actin cytoskeleton (Table S1) among cancer cells in "absent" tumors, with lower expression in "non-brisk" tumors, and even lower expression in "brisk" tumors (Figures 5H–5J and S6G). These results suggest that reduced immune pressure allows cancer cells to reach higher levels of stiffness and *SPP1* expression without being targeted for destruction, which is consistent with a role for *SPP1*-dependent mechanosurveillance in shaping the biophysical properties of human melanoma.

Spp1 mediates mechanoreciprocity and bone colonization

Having found that osteopontin promotes cell stiffness and mechanosurveillance, we next asked whether it might also influence mechanoreciprocity. $Spp1^{-/-}$ and $Spp1^{+/+}$ B16F10 cells were plated overnight on substrates of increasing rigidity, then subjected to SMR (Figure 6A). Whereas $Spp1^{+/+}$ cells stiffened in response to higher rigidity, both $Spp1^{-/-}$ cell lines exhibited little to no mechanical change (Figure 6B). These results indicated that osteopontin is crucial for B16F10 mechanoreciprocity and suggested a potential mechanism by which this protein might facilitate colonization of rigid microenvironments like the bone. To evaluate *in vivo* colonization directly, we injected Luc^{+} $Spp1^{-/-}$ or $Spp1^{+/+}$ B16F10 cells into WT or $Prf1^{-/-}$ mice (Figure 6C). As expected, $Spp1^{+/+}$ control cells colonized the lungs of WT recipients and both the lungs and femurs of $Prf1^{-/-}$ animals (Figures 6D, 6E, and S7A–S7C), indicative of a robust capacity for bone metastasis that is attenuated by cytotoxic lymphocytes. In contrast, $Spp1^{-/-}$ cells were unable to colonize the bone in either group of recipients. The same pattern of results was observed using NK cell-depleted mice and isotype antibody-treated controls; mice lacking NK cells developed $Spp1^{+/+}$ B16F10 metastases in the bone but did not support $Spp1^{-/-}$ colonization in this niche (Figures 6F–6H and S7D–S7F). Given that $Spp1^{-/-}$ B16F10 cells proliferate normally (Figure S5C), their inability to colonize the bone is unlikely to be caused by impaired post-seeding outgrowth. Rather, our data indicate that osteopontin is required for effective infiltration of, and biomechanical adaptation to, rigid microenvironments. In line with this interpretation, RNA-sequencing of $Spp1^{-/-}$ cells revealed decreased expression of genes related to the ECM, cytoskeletal remodeling, and adhesion (Figures S7G and S7H). Hence, *Spp1*-induced cell stiffening is coupled to a more adhesive and architecturally engaged state that may be necessary for bone metastasis.

To better define the role of osteopontin in bone colonization, we utilized a reconstitution system in which purified osteoblasts are cultured on a thin sheet of bone collagen (called demineralized bone paper [DBP]) (Figure 7A).[60] Over 7 days, the osteoblasts deposit mineral onto this substrate, generating a thin layer of optically transmissive bone that is amenable to live imaging. When added to these cultures after mineralization, B16F10 cells form colonies on the bone matrix that physically displace osteoblasts (Figure 7B). Under these conditions, $Spp1^{-/-}$ cells exhibited a significant growth defect relative to $Spp1^{+/+}$ controls (Figures 7B–7D). By contrast, both cell lines grew similarly on tissue culture plastic, indicative of a specific role for osteopontin in the colonization of mineralized DBP. These findings strongly suggest that cancer cell-intrinsic osteopontin facilitates interactions with the mineralized bone microenvironment.

Next, we applied spatial transcriptomics to determine where osteopontin might operate within *bona fide* bone metastases. Histological sections from two $Prf1^{-/-}$ bones bearing B16F10 tumors and one healthy $Prf1^{-/-}$ bone were analyzed using the Xenium 5K panel with custom add-on genes (Figure 7E; Table S2). After segmentation, several distinguishable cell types were identified by differential gene expression, including neutrophils, stromal cells, and an "osteolineage" group expressing genes characteristic of osteoblasts and osteoclasts (Figures 7F and S8A). To identify cancer cells, we developed a melanoma module containing four characteristic genes (*Pmel*, *Dct*, *Tyrp1*, and *Gpnmb*). By applying a threshold value for this metric that excluded 99.9% of cells from healthy bone, we delineated a transcriptomically diverse melanoma population (Figure 7G). Strong *Spp1* expression was detected within a subset of these cancer cells, which we renamed "*Spp1*-high B16 melanoma." Mapping cancer cells back onto the tissue, we found that *Spp1*-high melanoma cells were more likely than *Spp1*-low melanoma to colocalize with osteolineage cells (Figure 7H), an observation that we validated using cell neighborhood analysis with permutation testing (Figures 7I, S8B, and S8C). Osteolineage cells are key components of the endosteal niche, which lies at the interface between marrow and mineralized bone.[61] This niche was readily apparent in control sections, where osteolineage cells lined the trabecular and cortical bone surfaces, but was disrupted in metastatic samples, with cancer cells and osteolineage cells commingling close to several cortical bone surfaces and trabeculae (Figure 7H). To probe cell stiffness in this context, we developed a stiffness module using a set of established mechanical genes (Table S3). This module was elevated in osteolineage cells, as expected, but also in *Spp1*-high melanoma (Figure 7J). In spatial maps, high stiffness values were observed among cells lining the bone matrix and also where osteolineage cells colocalized with *Spp1*-high melanoma (Figures 7H and S8D), consistent with these two cell types engaging in mechanoreciprocal interactions

(E) SMR of the indicated MTCs from the indicated tumor-bearing mice. In (C) and (E), violins encompass the entire data distribution, with dashed lines denoting the median and dotted lines indicating the upper and lower quartiles. *p* values were calculated by one-way ANOVA, and samples sizes (*n*=) are displayed below each violin. Results are representative of at least two independent experiments.

(F–J) scRNA-seq analysis of cytoskeletal gene expression in a published cohort of melanoma patients.[44] (F) Schematic diagram illustrating the study design: melanoma biopsies from patients with the indicated immune infiltration states were analyzed.

(G and H) UMAP visualization of scRNA-seq data colored by patient ID (G) and immune infiltration state (H).

(I) *SPP1* gene expression in absent, non-brisk, and brisk tumors, calculated using data from pre-treatment samples.

(J) F-actin cytoskeleton gene expression in absent, non-brisk, and brisk tumors, calculated using data from pre-treatment samples. Module scores were generated using the KEGG "Regulation of Actin Cytoskeleton" pathway and a GSEA "Cytoskeleton" gene set (Table S1). In (H) and (I), embedded boxes indicate median and interquartile range. *p* values calculated by Wilcoxon rank-sum test.

See also Figures S4, S5, and S6.

Please cite this article in press as: Elbanna et al., Environmentally induced cell stiffening shapes metastatic site selection by tuning the immune vulnerability of cancer cells, Immunity (2026), https://doi.org/10.1016/j.immuni.2026.06.025

CellPress
OPEN ACCESS

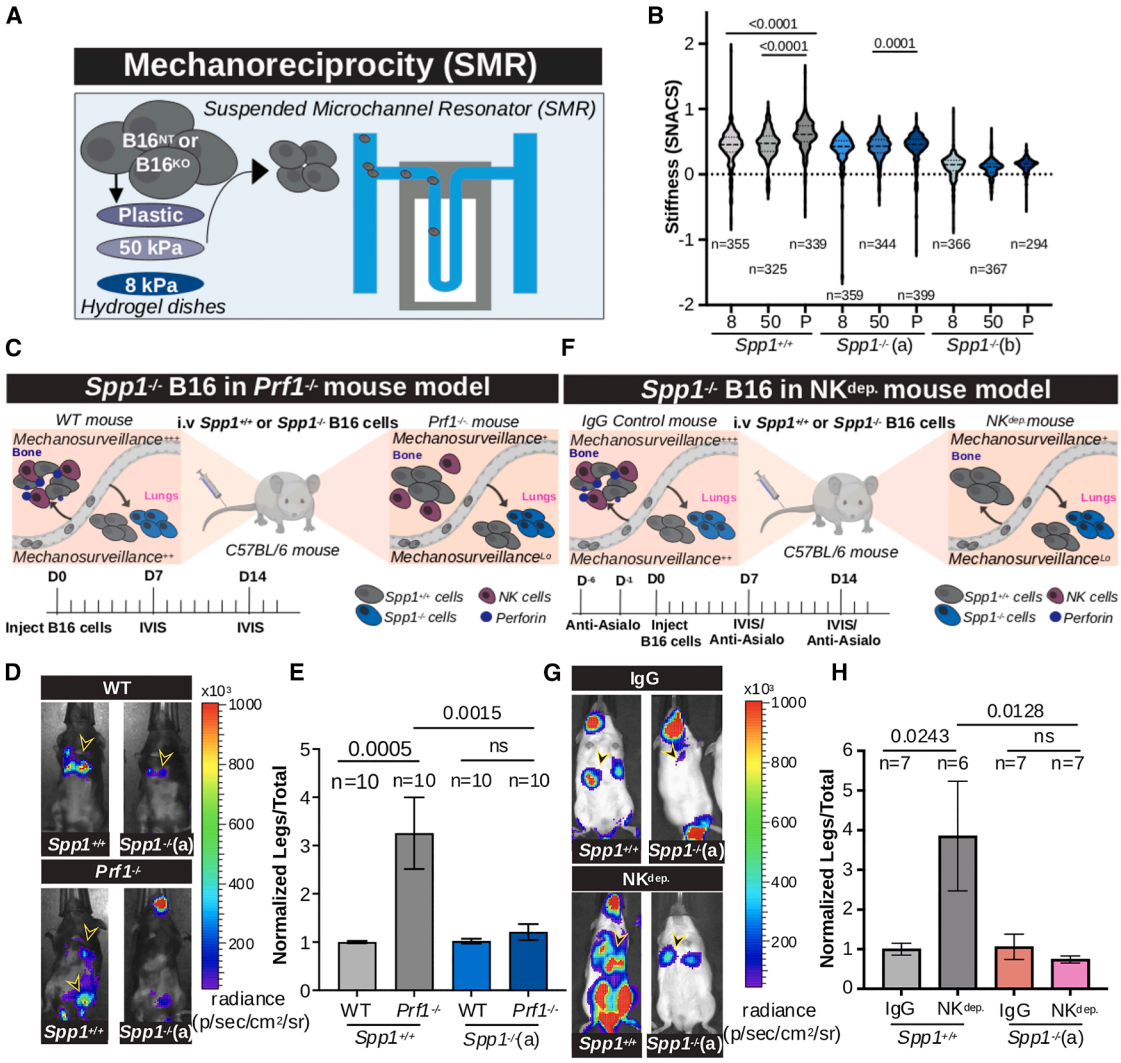

Figure 6. Cancer cell-derived *Spp1* mediates mechanoreciprocity and bone colonization

(A and B) *Spp1*$^{+/+}$ or *Spp1*$^{-/-}$ B16F10 cells were cultured overnight on substrates of differential rigidity and then subjected to SMR.

(A) Schematic diagram of the experimental approach.

(B) Stiffness measurements at the indicated substrate rigidities. P, plastic. Violins encompass the entire data distribution, with dashed lines denoting the median and dotted lines indicating the upper and lower quartiles. Samples sizes (n =) are displayed below each violin. p values calculated by one-way ANOVA. Results are representative of two independent experiments.

(C–H) Luc^{+} *Spp1*$^{+/+}$ or *Spp1*$^{-/-}$ B16F10 cells were injected i.v. into either WT and *Prf1*$^{-/-}$ mice (C–E) or into IgG control and NK depleted (NK$^{dep.}$) mice (F–H), which were then monitored for metastatic colonization of the lungs and bone. (C and F) Schematic diagrams of the experimental approach. (D and G) Representative bioluminescence images of tumor-bearing WT and *Prf1*$^{-/-}$ mice (D) or of IgG control and NK$^{dep.}$ mice (G) injected with the indicated B16F10 lines. (E and H) Quantification of relative femoral colonization, expressed as a normalized ratio of bioluminescence signal in the legs to the total bioluminescence signal. In (D) and (G), metastatic burden in the lungs and femurs is denoted by black and yellow arrowheads. In (E) and (H), Legs/Total ratios were pooled from two independent experiments. Error bars denote SEM, sample size is indicated above each bar, and p values were calculated by one-way ANOVA.

See also Figure S7.

in the endosteal niche. Collectively, these data identify osteopontin as a critical mechanoregulator of bone colonization.

DISCUSSION

In this study, we integrated biophysical assays, gene expression profiling, and *in vivo* models to demonstrate that environmental rigidity influences metastatic outgrowth through the coupled effects of mechanoreciprocity and mechanosurveillance. We also identified osteopontin as a critical, cancer cell-derived mediator of both processes. Importantly, transcriptional, biophysical, and histological analysis of patient samples indicated that the mechanoregulatory paradigm we established in mice also applies to humans. These results expand the scope of mechanobiology in metastasis and provide a framework for therapeutically targeting the interplay between mechanical adaptation and immunosurveillance.

It is now clear that tissues impose mechanical requirements for metastatic colonization.[10,62] However, whether these

Please cite this article in press as: Elbanna et al., Environmentally induced cell stiffening shapes metastatic site selection by tuning the immune vulnerability of cancer cells, Immunity (2026), https://doi.org/10.1016/j.immuni.2026.06.025

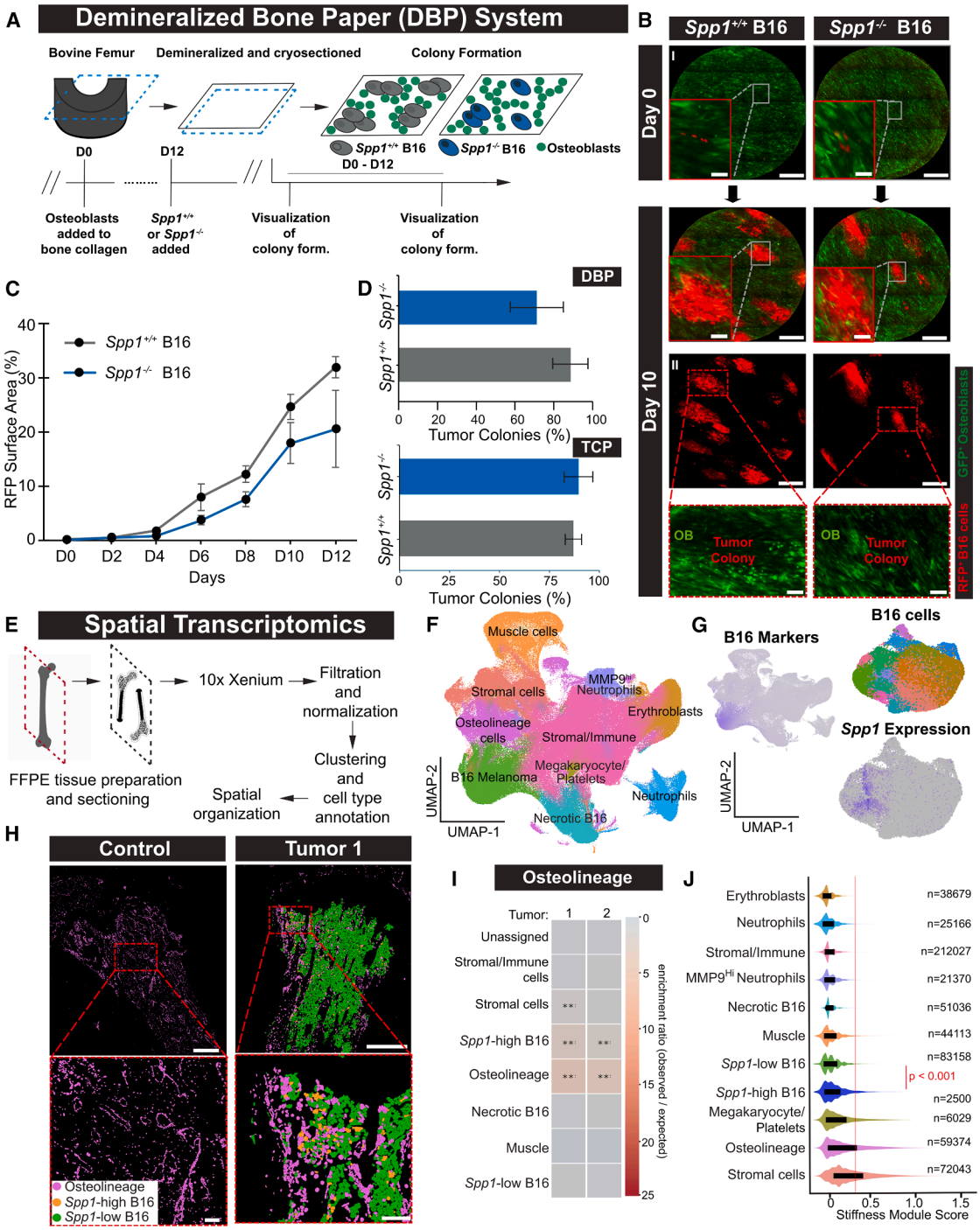

Figure 7. Cancer cell-derived *Spp1* enhances bone colonization and *in vivo* association with osteolineage cells

(A–D) *Spp1*$^{+/+}$ and *Spp1*$^{-/-}$ RFP^{+} B16F10 cells were added to reconstituted bone surfaces generated by culturing GFP^{+} murine osteoblasts on DBP. B16F10 colony formation and outgrowth were then monitored over time.

(A) Schematic diagram of the experimental workflow.

(B) Representative images of B16F10 colonies: (i) representative *Spp1*$^{+/+}$ and *Spp1*$^{-/-}$ colonies imaged at day 0 (above) and again at day 10 (below). Insets show magnified images of colonies of interest. (ii) Above, representative images of *Spp1*$^{+/+}$ and *Spp1*$^{-/-}$ B16F10 colonies. Below, magnified images of the regions boxed above, showing osteoblast displacement by B16F10 cells. Scale bars, 1,000 μm for main images, 100 μm for day 0 insets and 200 μm for day 10 insets.

(C and D) Quantification of B16F10 outgrowth by surface area coverage (C) and colony formation efficiency on DBP and tissue culture plastic (TCP) (D). Error bars denote standard deviation. *N* = 3 technical replicates.

(E–J) Xenium spatial transcriptomic analysis of healthy and tumor-bearing *Prf1*$^{-/-}$ bones.

(E) Schematic diagram of the experimental workflow.

(legend continued on next page)

Please cite this article in press as: Elbanna et al., Environmentally induced cell stiffening shapes metastatic site selection by tuning the immune vulnerability of cancer cells, Immunity (2026), https://doi.org/10.1016/j.immuni.2026.06.025

requirements are achieved via adaptation of cancer cells to their new environment or by selection of colonization-competent cells within the metastatic pool remains a point of contention. We have found that B16F10 cells mechanically adjust to substrate rigidity within 16 h, before substantial proliferation or cell death has occurred. Furthermore, *Spp1*$^{-/-}$ cells, which fail to mechanoreciprocate, also fail to colonize bone *in vivo*. These results indicate that mechanical adaptation to environmental rigidity is crucial for bone metastasis, at least in the experimental models used here. Although this interpretation does not rule out the importance of mechanical selection in stiff environments, it does imply that if such selection contributes, it is not selection for cell stiffness per se but rather for the capacity to stiffen in appropriate circumstances. Similarly, our results do not disprove the idea that metastatic preferences are imprinted by the biophysical properties of the primary tumor (termed "mechanical memory")[48,63,64]; they do suggest, however, that mechanical memory is not encoded directly in cytoskeletal architecture but rather the capacity of that architecture to respond to environmental rigidity. Hence, mechanical adaptability itself emerges as a critical selectable trait, supported by gene products like osteopontin, which enable cancer cells to mechanoreciprocate.

Bone is a highly nonuniform mechanical environment, with rigid trabeculae closely abutting soft bone marrow. The observation that osteopontin, which drives stiffening on rigid substrates, is required for bone colonization strongly suggests that mechanoreciprocity with its rigid, osseous components is an essential, early step in metastatic invasion. However, subsequent expansion into the marrow space would be expected to elicit a different mechanoreciprocal response, thereby increasing biomechanical variation within the metastasis. Our scRNA-seq, SMR, and spatial transcriptomic results are all consistent with this idea, revealing high transcriptomic and mechanical diversity among bone MTCs. Bone metastasis is thought to proceed via colonization of the endosteal niche, where cancer cells exploit osteoblast-derived signals and ECM components to anchor and proliferate.[61,65,66] We posit that osteopontin-dependent mechanoreciprocity enables the integration of *Spp1*-high cancer cells into this microenvironment while concomitantly sensitizing them to mechanosurveillance. Thus, while the endosteal niche serves as a favorable environment for initial colonization, it may also impose biophysical constraints that limit immune evasion.

Although osteopontin has long been associated with bone metastasis,[50–59] how it promotes colonization of the endosteal niche remains unresolved. Our results establish a biomechanical basis for osteopontin activity, demonstrating not only that it is induced in stiff environments but also that it enables cancer cells to sense these environments. Given that osteopontin is secreted, it is tempting to speculate that it functions as an "adhesion adaptor," enabling cancer cells that express osteopontin receptors to better adhere and respond to bone matrix. A role for secreted osteopontin as an adhesion adaptor is consistent with prior studies showing that *Spp1* promotes osteoclast binding to bone matrix and that osteopontin accumulates at the interface between cancer cells and mineral bone in human metastases.[46,47,67] The question remains why cancer cells must express their own osteopontin, rather than exploit the presumably abundant osteopontin produced by other bone resident cells. It is possible that cancer cell-extrinsic pools of osteopontin are bound by other cells or sequestered in microenvironments that are inaccessible or inhospitable to cancer cells. Experiments targeting specific sources and isoforms of osteopontin will be necessary to address this issue.

Osteopontin is known to inhibit CTL activation by engaging CD44, a cell surface receptor expressed by both T cells and NK cells.[68,69] This immunosuppressive mechanism contrasts with our results indicating that osteopontin mechanically sensitizes MTCs to cytotoxic lymphocytes. Whether the activating or the inhibitory mechanism predominates likely depends on contextual factors such as environmental rigidity, the abundance of osteopontin, and its accessibility to cancer cells and cytotoxic lymphocytes. The capacity of osteopontin to promote tumor fitness while simultaneously modulating cytotoxic lymphocyte function in opposing directions will likely complicate efforts to target the protein therapeutically. Mechanistically decoupling the immunosuppressive and mechanoregulatory activities of osteopontin could enable investigators to leverage its immunostimulatory benefits while simultaneously avoiding lymphocyte suppression.

Cancer vulnerabilities canonically exhibit two key properties: first, they are required for disease progression, and second, they are specific to cancer cells. Mechanoreciprocal stiffening in rigid microenvironments satisfies the first criterion because it is a necessary step in metastatic progression. This behavior is not unique to cancer cells, however, raising the question of how it might serve as a specific trigger for antitumor immunosurveillance. The answer likely lies in the combinatorial nature of immune recognition. In metastatic cells, mechanoreciprocal stiffening occurs in the context of a permissive constellation of surface ligands that is presumably not present in other bone-resident cell types. This allows an otherwise normal biophysical feature to become a differential index of dysregulation that triggers cytotoxic lymphocyte attack. Hence, by combining mechanosensing with multimodal molecular recognition, immune cells expand both the scope and the specificity of their surveillance function.

Limitations of the study

We employed young adult mice (6–8 weeks) for our *in vivo* metastasis experiments, which is a standard approach in the field because bone colonization is much more challenging to

(F) UMAP plot containing all segmented cells pooled from all samples, labeled for cell identity.
(G) Left, feature plot showing expression of a melanoma module score comprising *Dct*, *Tyrp1*, *Pmel*, and *Gpnmb*. Right, cells with high melanoma module scores were reprojected into UMAP space. Seurat clustering is shown above, and an *Spp1* feature plot below.
(H) Representative images of tumor-bearing and control (uninjected) bones showing *Spp1*-high B16F10 cells (orange), *Spp1*-low B16F10 cells (green), and osteolineage cells (purple). Insets show higher magnification views of the boxed areas above. Scale bar, 500 μm in the main images, 100 μm in the insets.
(I) The spatial proximity of each cell type to osteolineage cells, expressed as a ratio of observed to expected distance. *** denotes $p < 0.001$, calculated by permutation test.
(J) A stiffness module score was calculated for each cell based on its expression of 79 stiffness-related genes (Table S3), and the results graphed by cell identity. Embedded boxes indicate median and interquartile range.
See also Figure S8.

induce in older (e.g., 15 weeks) animals.[70–72] The increased susceptibility of younger mice has been attributed to their higher levels of bone remodeling,[70] which is intriguing in light of emerging links between bone destabilization and bone metastasis in the clinic.[73,74] That being said, bone metastasis typically occurs in older patients, and in that regard our experimental model may not recapitulate certain aspects of the clinically relevant bone microenvironment. While our results strongly suggest that cytotoxic lymphocytes are the direct mediators of mechanosurveillance in our model system, we have not exhaustively ruled out a contribution from myeloid cells, which could potentially shape the survival and mechanical properties of MTCs downstream of lymphocyte cytokine or chemokine release. Cell stiffness is influenced both by the cortical cytoskeleton and by plasma membrane mechanics.[75] The relative contribution of each to MTC mechanoreciprocity remains an unresolved question, and addressing it will likely require approaches capable of experimentally decoupling the plasma membrane from the underlying F-actin cortex. Finally, although the inverse correlation of immune infiltration with *SPP1* and cytoskeletal gene expression that we observed in patient melanoma is consistent with the preferential destruction of stiffer cancer cells by cytotoxic lymphocytes, other possible explanations, including *SPP1* and cytoskeletally dependent inhibition of immune infiltration and/or function, have not been ruled out.

RESOURCE AVAILABILITY

Lead contact

Requests for information and reagents should be directed to Morgan Huse (husem@mskcc.org).

Materials availability

The materials associated with this study are available upon request, except for the patient spinal metastasis samples, which are unique biological resources. Histological images of these tissues are, however, available.

Data and code availability

The bulk RNA-seq data generated in this study have been deposited in the Gene Expression Omnibus under accession GEO: GSE330079. The single-cell RNA-seq data have been deposited under accession GEO: GSE331042, and the spatial transcriptomics data have been deposited under accession GEO: GSE329415. Single-cell RNA-seq analysis code is available at GitHub: https://github.com/ElbannaYassmin/Single-Cell-RNA-sequencing-analysis-of-WT-vs-PRF1——B16F10-injected-mice, and spatial transcriptomics analysis code is available at GitHub: https://github.com/ElbannaYassmin/Spatial-Transcriptomics-of-bone-tissue-PRF1——B16F10-injected-mice-vs-healthy-controls. The bulk RNA-seq analysis workflow is described at https://soccin.github.io/pwg-docs/methods/rnaSeq.html. All accession numbers and code repositories will be publicly accessible upon publication. All other source data are available upon request.

ACKNOWLEDGMENTS

We thank Z. Eraslan and J. Zippin for assistance with CRISPR-Cas9-based deletion; K. Ganesh and A. Boire for reagents; P. Manoj, A. Shoenfeld, C. Rudin, N. Socci, X. Xiang, J. Silber, J. Wolchok, and T. Merghoub for help with patient data; the MSKCC Flow Cytometry Core for assistance with FACS; the MSKCC Molecular Cytology Core for assistance with imaging and AFM; the MSKCC Integrated Genomics Operation for assistance with bulk RNA-seq, scRNA-seq, and spatial transcriptomics; T. Tammela and A. Boire for critical reading of the manuscript; and members of the M. Huse lab for advice. The study was supported in part by the US National Institutes of Health (R01-CA286566 to M.H., R01-AI087644 to M.H., P30-CA008748 to MSKCC, P30-CA014051 to MIT, F31-CA294974 to Y.A.E., R01-CA237171 to J.L., and R35-CA252978 to J.M.), the Alan and Sandra Gerry Metastasis and Tumor Ecosystems Center (M.H.), the Ludwig Center for Cancer Immunotherapy (M.T.-L. and B.Y.W.), the D. K. Ludwig Fund for Cancer Research (S.R.M.), the Tow Center for Developmental Oncology (M.H.), and the Cancer Research Institute (B.Y.W.).

AUTHOR CONTRIBUTIONS

Y.A.E., M.T.-L., A.H., Y.Z., C. Li, S.A., E.L., B.Y.W., C. Leslie, J.L., O.B., S.R.M., and M.H. designed the experiments. Y.A.E., M.T.-L., A.H., Y.Z., S.A., E. Lee, Z.W., A.Y., A.V., M.D., S.V., S.M.D., J.B., N.F., Y.H.K., T.A.B., and M.H. collected the data. Y.A.E., M.T.-L., A.H., Y.Z., C. Li, S.A., E. Ladewig, Y.H.K., T.A.B., E. Lee, K.K.H.Y., C. Leslie, O.B., and M.H. analyzed the data. Z.W., J.-G.K., and J.L. provided critical reagents. C. Leslie, J.M., J.L., S.R.M., and M.H. provided research support. Y.A.E. and M.H. wrote the paper with input from A.H., Z.W., K.K.H.Y., J.M., J.L., O.B., and S.R.M.

DECLARATION OF INTERESTS

S.R.M. is a founder of Travera and of Affinity Biosensors. J.M. owns company stock in Scholar Rock.

STAR★METHODS

Detailed methods are provided in the online version of this paper and include the following:

SUPPLEMENTAL INFORMATION

Supplemental information can be found online at https://doi.org/10.1016/j.immuni.2026.06.025.

Received: June 17, 2025
Revised: February 2, 2026
Accepted: June 30, 2026

REFERENCES

1. Dillekås, H., Rogers, M.S., and Straume, O. (2019 Sep). Are 90% of deaths from cancer caused by metastases? Cancer Med *8* (12), 5574–5576. https://doi.org/10.1002/cam4.2474.
2. Nguyen, D.X., Bos, P.D., and Massagué, J. (2009). Metastasis: from dissemination to organ-specific colonization. Nat. Rev. Cancer *9*, 274–284. https://doi.org/10.1038/nrc2622.
3. Fares, J., Fares, M.Y., Khachfe, H.H., Salhab, H.A., and Fares, Y. (2020). Molecular principles of metastasis: a hallmark of cancer revisited. Signal Transduct. Target. Ther. *5*, 28. https://doi.org/10.1038/s41392-020-0134-x.
4. Seyfried, T.N., and Huysentruyt, L.C. (2013). On the origin of cancer metastasis. Crit. Rev. Oncog. *18*, 43–73. https://doi.org/10.1615/critrevoncog.v18.i1-2.40.
5. Patras, L., Shaashua, L., Matei, I., and Lyden, D. (2023). Immune determinants of the pre-metastatic niche. Cancer Cell *41*, 546–572. https://doi.org/10.1016/j.ccell.2023.02.018.
6. Guimarães, C.F., Gasperini, L., Marques, A.P., and Reis, R.L. (2020). The stiffness of living tissues and its implications for tissue engineering. Nat. Rev. Mater. *5*, 351–370. https://doi.org/10.1038/s41578-019-0169-1.
7. Iskratsch, T., Wolfenson, H., and Sheetz, M.P. (2014). Appreciating force and shape-the rise of mechanotransduction in cell biology. Nat. Rev. Mol. Cell Biol. *15*, 825–833. https://doi.org/10.1038/nrm3903.
8. Paszek, M.J., and Weaver, V.M. (2004). The tension mounts: mechanics meets morphogenesis and malignancy. J. Mammary Gland Biol. Neoplasia *9*, 325–342. https://doi.org/10.1007/s10911-004-1404-x.
9. Butcher, D.T., Alliston, T., and Weaver, V.M. (2009). A tense situation: forcing tumour progression. Nat. Rev. Cancer *9*, 108–122. https://doi.org/10.1038/nrc2544.
10. Agrawal, A., Javanmardi, Y., Watson, S.A., Serwinski, B., Djordjevic, B., Li, W., Aref, A.R., Jenkins, R.W., and Moeendarbary, E. (2025). Mechanical signatures in cancer metastasis. NPJ Biol. Phys Mech. *2*, 3. https://doi.org/10.1038/s44341-024-00007-x.
11. Solon, J., Levental, I., SenGupta, K., Georges, P.C., and Janmey, P.A. (2007). Fibroblast adaptation and stiffness matching to soft elastic substrates. Biophys. J. *93*, 4453–4461. https://doi.org/10.1529/biophysj.106.101386.
12. Byfield, F.J., Reen, R.K., Shentu, T.P., Levitan, I., and Gooch, K.J. (2009). Endothelial actin and cell stiffness is modulated by substrate stiffness in 2D and 3D. J. Biomech. *42*, 1114–1119. https://doi.org/10.1016/j.jbiomech.2009.02.012.
13. Guo, M., Pegoraro, A.F., Mao, A., Zhou, E.H., Arany, P.R., Han, Y., Burnette, D.T., Jensen, M.H., Kasza, K.E., Moore, J.R., et al. (2017). Cell volume change through water efflux impacts cell stiffness and stem cell fate. Proc. Natl. Acad. Sci. USA *114*, E8618–E8627. https://doi.org/10.1073/pnas.1705179114.
14. Pelham, R.J., Jr., and Wang, Yl. (1997). Cell locomotion and focal adhesions are regulated by substrate flexibility. Proc. Natl. Acad. Sci. USA *94*, 13661–13665. https://doi.org/10.1073/pnas.94.25.13661.
15. Finn, O.J. (2018). A Believer's Overview of Cancer Immunosurveillance and Immunotherapy. J. Immunol. *200*, 385–391. https://doi.org/10.4049/jimmunol.1701302.
16. Janssen, L.M.E., Ramsay, E.E., Logsdon, C.D., and Overwijk, W.W. (2017). The immune system in cancer metastasis: friend or foe? J. Immunother. Cancer *5*, 79. https://doi.org/10.1186/s40425-017-0283-9.
17. Xie, N., Shen, G., Gao, W., Huang, Z., Huang, C., and Fu, L. (2023). Neoantigens: promising targets for cancer therapy. Signal Transduct. Target. Ther. *8*, 9. https://doi.org/10.1038/s41392-022-01270-x.
18. Lanier, L.L. (2005). NK cell recognition. Annu. Rev. Immunol. *23*, 225–274. https://doi.org/10.1146/annurev.immunol.23.021704.115526.
19. Dustin, M.L., and Long, E.O. (2010). Cytotoxic immunological synapses. Immunol. Rev. *235*, 24–34. https://doi.org/10.1111/j.0105-2896.2010.00904.x.
20. Wei, S.C., Duffy, C.R., and Allison, J.P. (2018). Fundamental Mechanisms of Immune Checkpoint Blockade Therapy. Cancer Discov. *8*, 1069–1086. https://doi.org/10.1158/2159-8290.CD-18-0367.
21. Basu, R., and Huse, M. (2017). Mechanical Communication at the Immunological Synapse. Trends Cell Biol. *27*, 241–254. https://doi.org/10.1016/j.tcb.2016.10.005.
22. Chen, W., Lou, J., and Zhu, C. (2010). Forcing switch from short- to intermediate- and long-lived states of the alphaA domain generates LFA-1/ICAM-1 catch bonds. J. Biol. Chem. *285*, 35967–35978. https://doi.org/10.1074/jbc.M110.155770.
23. González, C., Chames, P., Kerfelec, B., Baty, D., Robert, P., and Limozin, L. (2019). Nanobody-CD16 Catch Bond Reveals NK Cell Mechanosensitivity. Biophys. J. *116*, 1516–1526. https://doi.org/10.1016/j.bpj.2019.03.012.
24. Liu, B., Chen, W., Evavold, B.D., and Zhu, C. (2014). Accumulation of dynamic catch bonds between TCR and agonist peptide-MHC triggers T cell signaling. Cell *157*, 357–368. https://doi.org/10.1016/j.cell.2014.02.053.
25. Blumenthal, D., Chandra, V., Avery, L., and Burkhardt, J.K. (2020). Mouse T cell priming is enhanced by maturation-dependent stiffening of the dendritic cell cortex. eLife *9*, e55995. https://doi.org/10.7554/eLife.55995.
26. Judokusumo, E., Tabdanov, E., Kumari, S., Dustin, M.L., and Kam, L.C. (2012). Mechanosensing in T lymphocyte activation. Biophys. J. *102*, L5–L7. https://doi.org/10.1016/j.bpj.2011.12.011.
27. Saitakis, M., Dogniaux, S., Goudot, C., Bufi, N., Asnacios, S., Maurin, M., Randriamampita, C., Asnacios, A., and Hivroz, C. (2017). Different TCR-induced T lymphocyte responses are potentiated by stiffness with variable sensitivity. eLife *6*, e23190. https://doi.org/10.7554/eLife.23190.
28. Wan, Z., Zhang, S., Fan, Y., Liu, K., Du, F., Davey, A.M., Zhang, H., Han, W., Xiong, C., and Liu, W. (2013). B cell activation is regulated by the stiffness properties of the substrate presenting the antigens. J. Immunol. *190*, 4661–4675. https://doi.org/10.4049/jimmunol.1202976.
29. Tello-Lafoz, M., Srpan, K., Sanchez, E.E., Hu, J., Remsik, J., Romin, Y., Calò, A., Hoen, D., Bhanot, U., Morris, L., et al. (2021). Cytotoxic lymphocytes target characteristic biophysical vulnerabilities in cancer. Immunity *54*, 1037–1054.e7. https://doi.org/10.1016/j.immuni.2021.02.020.
30. Lei, K., Kurum, A., Kaynak, M., Bonati, L., Han, Y., Cencen, V., Gao, M., Xie, Y.Q., Guo, Y., Hannebelle, M.T.M., et al. (2021). Cancer-cell stiffening via cholesterol depletion enhances adoptive T-cell immunotherapy. Nat. Biomed. Eng. *5*, 1411–1425. https://doi.org/10.1038/s41551-021-00826-6.
31. Liu, Y., Zhang, T., Zhang, H., Li, J., Zhou, N., Fiskesund, R., Chen, J., Lv, J., Ma, J., Zhang, H., et al. (2021). Cell Softness Prevents Cytolytic T-cell Killing of Tumor-Repopulating Cells. Cancer Res. *81*, 476–488. https://doi.org/10.1158/0008-5472.CAN-20-2569.
32. Kang, J.H., Miettinen, T.P., Chen, L., Olcum, S., Katsikis, G., Doyle, P.S., and Manalis, S.R. (2019). Publisher Correction: noninvasive monitoring of single-cell mechanics by acoustic scattering. Nat. Methods *16*, 270. https://doi.org/10.1038/s41592-019-0354-6.
33. Jordan, M.B., Hildeman, D., Kappler, J., and Marrack, P. (2004). An animal model of hemophagocytic lymphohistiocytosis (HLH): CD8+ T cells and interferon gamma are essential for the disorder. Blood *104*, 735–743. https://doi.org/10.1182/blood-2003-10-3413.
34. Badovinac, V.P., Hamilton, S.E., and Harty, J.T. (2003). Viral infection results in massive CD8+ T cell expansion and mortality in vaccinated perforin-deficient mice. Immunity *18*, 463–474. https://doi.org/10.1016/s1074-7613(03)00079-7.
35. Binder, D., van den Broek, M.F., Kägi, D., Bluethmann, H., Fehr, J., Hengartner, H., and Zinkernagel, R.M. (1998). Aplastic anemia rescued by exhaustion of cytokine-secreting CD8+ T cells in persistent infection with lymphocytic choriomeningitis virus. J. Exp. Med. *187*, 1903–1920. https://doi.org/10.1084/jem.187.11.1903.

36. Meeth, K., Wang, J.X., Micevic, G., Damsky, W., and Bosenberg, M.W. (2016). The YUMM lines: a series of congenic mouse melanoma cell lines with defined genetic alterations. Pigment Cell Melanoma Res. *29*, 590–597. https://doi.org/10.1111/pcmr.12498.

37. Yadav, M., Jhunjhunwala, S., Phung, Q.T., Lupardus, P., Tanguay, J., Bumbaca, S., Franci, C., Cheung, T.K., Fritsche, J., Weinschenk, T., et al. (2014). Predicting immunogenic tumour mutations by combining mass spectrometry and exome sequencing. Nature *515*, 572–576. https://doi.org/10.1038/nature14001.

38. Carpenter, R.A., Kwak, J.G., Peyton, S.R., and Lee, J. (2018). Implantable pre-metastatic niches for the study of the microenvironmental regulation of disseminated human tumour cells. Nat. Biomed. Eng. *2*, 915–929. https://doi.org/10.1038/s41551-018-0307-x.

39. Alexandrov, L.B., Nik-Zainal, S., Wedge, D.C., Aparicio, S.A.J.R., Behjati, S., Biankin, A.V., Bignell, G.R., Bolli, N., Borg, A., Børresen-Dale, A.L., et al. (2013). Signatures of mutational processes in human cancer. Nature *500*, 415–421. https://doi.org/10.1038/nature12477.

40. Zhang, J., Huang, D., Saw, P.E., and Song, E. (2022). Turning cold tumors hot: from molecular mechanisms to clinical applications. Trends Immunol. *43*, 523–545. https://doi.org/10.1016/j.it.2022.04.010.

41. Gan, S., Macalinao, D.G., Shahoei, S.H., Tian, L., Jin, X., Basnet, H., Bibby, C., Muller, J.T., Atri, P., Seffar, E., et al. (2024). Distinct tumor architectures and microenvironments for the initiation of breast cancer metastasis in the brain. Cancer Cell *42*, 1693–1712.e24. https://doi.org/10.1016/j.ccell.2024.08.015.

42. Ning, J., Ye, Y., Shen, H., Zhang, R., Li, H., Song, T., Zhang, R., Liu, P., Chen, G., Wang, H., et al. (2024). Macrophage-coated tumor cluster aggravates hepatoma invasion and immunotherapy resistance via generating local immune deprivation. Cell Rep. Med. *5*, 101505. https://doi.org/10.1016/j.xcrm.2024.101505.

43. Qian, B., Deng, Y., Im, J.H., Muschel, R.J., Zou, Y., Li, J., Lang, R.A., and Pollard, J.W. (2009). A distinct macrophage population mediates metastatic breast cancer cell extravasation, establishment and growth. PLOS One *4*, e6562. https://doi.org/10.1371/journal.pone.0006562.

44. Pozniak, J., Pedri, D., Landeloos, E., Van Herck, Y., Antoranz, A., Vanwynsberghe, L., Nowosad, A., Roda, N., Makhzami, S., Bervoets, G., et al. (2024). A TCF4-dependent gene regulatory network confers resistance to immunotherapy in melanoma. Cell *187*, 166–183.e25. https://doi.org/10.1016/j.cell.2023.11.037.

45. Bastos, A.C.S.D.F., Gomes, A.V.P., Silva, G.R., Emerenciano, M., Ferreira, L.B., and Gimba, E.R.P. (2023). The Intracellular and Secreted Sides of Osteopontin and Their Putative Physiopathological Roles. Int. J. Mol. Sci. *24*, 2942. https://doi.org/10.3390/ijms24032942.

46. Asou, Y., Rittling, S.R., Yoshitake, H., Tsuji, K., Shinomiya, K., Nifuji, A., Denhardt, D.T., and Noda, M. (2001). Osteopontin facilitates angiogenesis, accumulation of osteoclasts, and resorption in ectopic bone. Endocrinology *142*, 1325–1332. https://doi.org/10.1210/endo.142.3.8006.

47. Chellaiah, M.A., Kizer, N., Biswas, R., Alvarez, U., Strauss-Schoenberger, J., Rifas, L., Rittling, S.R., Denhardt, D.T., and Hruska, K.A. (2003). Osteopontin deficiency produces osteoclast dysfunction due to reduced CD44 surface expression. Mol. Biol. Cell *14*, 173–189. https://doi.org/10.1091/mbc.e02-06-0354.

48. Watson, A.W., Grant, A.D., Parker, S.S., Hill, S., Whalen, M.B., Chakrabarti, J., Harman, M.W., Roman, M.R., Forte, B.L., Gowan, C.C., et al. (2021). Breast tumor stiffness instructs bone metastasis via maintenance of mechanical conditioning. Cell Rep. *35*, 109293. https://doi.org/10.1016/j.celrep.2021.109293.

49. You, Y., Zheng, Q., Dong, Y., Wang, Y., Zhang, L., Xue, T., Xie, X., Hu, C., Wang, Z., Chen, R., et al. (2015). Higher Matrix Stiffness Upregulates Osteopontin Expression in Hepatocellular Carcinoma Cells Mediated by Integrin β1/GSK3β/β-Catenin Signaling Pathway. PLOS One *10*, e0134243. https://doi.org/10.1371/journal.pone.0134243.

50. Kang, Y., Siegel, P.M., Shu, W., Drobnjak, M., Kakonen, S.M., Cordón-Cardo, C., Guise, T.A., and Massagué, J. (2003). A multigenic program mediating breast cancer metastasis to bone. Cancer Cell *3*, 537–549. https://doi.org/10.1016/s1535-6108(03)00132-6.

51. Bhattacharya, S.D., Mi, Z., Kim, V.M., Guo, H., Talbot, L.J., and Kuo, P.C. (2012). Osteopontin regulates epithelial mesenchymal transition-associated growth of hepatocellular cancer in a mouse xenograft model. Ann. Surg. *255*, 319–325. https://doi.org/10.1097/SLA.0b013e31823e3a1c.

52. Kovacheva, M., Zepp, M., Schraad, M., Berger, S., and Berger, M.R. (2019). Conditional Knockdown of Osteopontin Inhibits Breast Cancer Skeletal Metastasis. Int. J. Mol. Sci. *20*, 4918. https://doi.org/10.3390/ijms20194918.

53. Zhao, Y., Bachelier, R., Treilleux, I., Pujuguet, P., Peyruchaud, O., Baron, R., Clément-Lacroix, P., and Clézardin, P. (2007). Tumor alphavbeta3 integrin is a therapeutic target for breast cancer bone metastases. Cancer Res. *67*, 5821–5830. https://doi.org/10.1158/0008-5472.CAN-06-4499.

54. Nemoto, H., Rittling, S.R., Yoshitake, H., Furuya, K., Amagasa, T., Tsuji, K., Nifuji, A., Denhardt, D.T., and Noda, M. (2001). Osteopontin deficiency reduces experimental tumor cell metastasis to bone and soft tissues. J. Bone Miner. Res. *16*, 652–659. https://doi.org/10.1359/jbmr.2001.16.4.652.

55. Hotte, S.J., Winquist, E.W., Stitt, L., Wilson, S.M., and Chambers, A.F. (2002). Plasma osteopontin: associations with survival and metastasis to bone in men with hormone-refractory prostate carcinoma. Cancer *95*, 506–512. https://doi.org/10.1002/cncr.10709.

56. Pang, X., Zhang, J., He, X., Gu, Y., Qian, B.Z., Xie, R., Yu, W., Zhang, X., Li, T., Shi, X., et al. (2021). SPP1 Promotes Enzalutamide Resistance and Epithelial-Mesenchymal-Transition Activation in Castration-Resistant Prostate Cancer via PI3K/AKT and ERK1/2 Pathways. Oxid. Med. Cell. Longev. *2021*, 5806602. https://doi.org/10.1155/2021/5806602.

57. Hou, X., Wu, X., Huang, P., Zhan, J., Zhou, T., Ma, Y., Qin, T., Luo, R., Feng, Y., Xu, Y., et al. (2015). Osteopontin is a useful predictor of bone metastasis and survival in patients with locally advanced nasopharyngeal carcinoma. Int. J. Cancer *137*, 1672–1678. https://doi.org/10.1002/ijc.29540.

58. Singhal, H., Bautista, D.S., Tonkin, K.S., O'Malley, F.P., Tuck, A.B., Chambers, A.F., and Harris, J.F. (1997). Elevated plasma osteopontin in metastatic breast cancer associated with increased tumor burden and decreased survival. Clin. Cancer Res. *3*, 605–611.

59. Carlinfante, G., Vassiliou, D., Svensson, O., Wendel, M., Heinegård, D., and Andersson, G. (2003). Differential expression of osteopontin and bone sialoprotein in bone metastasis of breast and prostate carcinoma. Clin. Exp. Metastasis *20*, 437–444. https://doi.org/10.1023/a:1025419708343.

60. Park, Y., Sato, T., and Lee, J. (2023). Functional and analytical recapitulation of osteoclast biology on demineralized bone paper. Nat. Commun. *14*, 8092. https://doi.org/10.1038/s41467-023-44000-9.

61. Muscarella, A.M., Aguirre, S., Hao, X., Waldvogel, S.M., and Zhang, X.H.F. (2021). Exploiting bone niches: progression of disseminated tumor cells to metastasis. J. Clin. Investig. *131*, e143764. https://doi.org/10.1172/JCI143764.

62. Er, E.E., Tello-Lafoz, M., and Huse, M. (2022). Mechanoregulation of Metastasis beyond the Matrix. Cancer Res. *82*, 3409–3419. https://doi.org/10.1158/0008-5472.CAN-22-0419.

63. Nasrollahi, S., Walter, C., Loza, A.J., Schimizzi, G.V., Longmore, G.D., and Pathak, A. (2017). Past matrix stiffness primes epithelial cells and regulates their future collective migration through a mechanical memory. Biomaterials *146*, 146–155. https://doi.org/10.1016/j.biomaterials.2017.09.012.

64. Yang, C., Tibbitt, M.W., Basta, L., and Anseth, K.S. (2014). Mechanical memory and dosing influence stem cell fate. Nat. Mater. *13*, 645–652. https://doi.org/10.1038/nmat3889.

65. Haider, M.T., Smit, D.J., and Taipaleenmäki, H. (2020). The Endosteal Niche in Breast Cancer Bone Metastasis. Front. Oncol. *10*, 335. https://doi.org/10.3389/fonc.2020.00335.

66. Wang, H., Yu, C., Gao, X., Welte, T., Muscarella, A.M., Tian, L., Zhao, H., Zhao, Z., Du, S., Tao, J., et al. (2015). The osteogenic niche promotes early-stage bone colonization of disseminated breast cancer cells. Cancer Cell *27*, 193–210. https://doi.org/10.1016/j.ccell.2014.11.017.

67. Ibrahim, T., Leong, I., Sanchez-Sweatman, O., Khokha, R., Sodek, J., Tenenbaum, H.C., Ganss, B., and Cheifetz, S. (2000). Expression of bone sialoprotein and osteopontin in breast cancer bone metastases. Clin. Exp. Metastasis *18*, 253–260. https://doi.org/10.1023/a:1006754605901.

68. Klement, J.D., Paschall, A.V., Redd, P.S., Ibrahim, M.L., Lu, C., Yang, D., Celis, E., Abrams, S.I., Ozato, K., and Liu, K. (2018). An osteopontin/CD44 immune checkpoint controls CD8+ T cell activation and tumor immune evasion. J. Clin. Investig. *128*, 5549–5560. https://doi.org/10.1172/JCI123360.

69. Klement, J.D., Poschel, D.B., Lu, C., Merting, A.D., Yang, D., Redd, P.S., and Liu, K. (2021). Osteopontin Blockade Immunotherapy Increases Cytotoxic T Lymphocyte Lytic Activity and Suppresses Colon Tumor Progression. Cancers (Basel) *13*, 1006. https://doi.org/10.3390/cancers13051006.

70. Wang, N., Reeves, K.J., Brown, H.K., Fowles, A.C.M., Docherty, F.E., Ottewell, P.D., Croucher, P.I., Holen, I., and Eaton, C.L. (2015). The frequency of osteolytic bone metastasis is determined by conditions of the soil, not the number of seeds; evidence from in vivo models of breast and prostate cancer. J. Exp. Clin. Cancer Res. *34*, 124. https://doi.org/10.1186/s13046-015-0240-8.

71. Bandyopadhyay, A., Elkahloun, A., Baysa, S.J., Wang, L., and Sun, L.Z. (2005). Development and gene expression profiling of a metastatic variant of the human breast cancer MDA-MB-435 cells. Cancer Biol. Ther. *4*, 168–174. https://doi.org/10.4161/cbt.4.2.1436.

72. Yu, Y., Li, K., Peng, Y., Wu, W., Chen, F., Shao, Z., and Zhang, Z. (2023). Animal models of cancer metastasis to the bone. Front. Oncol. *13*, 1165380. https://doi.org/10.3389/fonc.2023.1165380.

73. Salamanna, F., Borsari, V., Contartese, D., Nicoli Aldini, N., and Fini, M. (2018). Link between estrogen deficiency osteoporosis and susceptibility to bone metastases: A way towards precision medicine in cancer patients. Breast *41*, 42–50. https://doi.org/10.1016/j.breast.2018.06.013.

74. Kremer, R., Gagnon, B., Meguerditchian, A.N., Nadeau, L., and Mayo, N. (2014). Effect of oral bisphosphonates for osteoporosis on development of skeletal metastases in women with breast cancer: results from a pharmaco-epidemiological study. J. Natl. Cancer Inst. *106*, dju264. https://doi.org/10.1093/jnci/dju264.

75. Galie, P.A., Georges, P.C., and Janmey, P.A. (2022). How do cells stiffen? Biochem. J. *479*, 1825–1842. https://doi.org/10.1042/Bcj20210806.

76. Hoadley, K.A., Yau, C., Hinoue, T., Wolf, D.M., Lazar, A.J., Drill, E., Shen, R., Taylor, A.M., Cherniack, A.D., Thorsson, V., et al. (2018). Cell-of-Origin Patterns Dominate the Molecular Classification of 10,000 Tumors from 33 Types of Cancer. Cell *173*, 291–304.e6. https://doi.org/10.1016/j.cell.2018.03.022.

77. Er, E.E., Valiente, M., Ganesh, K., Zou, Y., Agrawal, S., Hu, J., Griscom, B., Rosenblum, M., Boire, A., Brogi, E., et al. (2018). Pericyte-like spreading by disseminated cancer cells activates YAP and MRTF for metastatic colonization. Nat. Cell Biol. *20*, 966–978. https://doi.org/10.1038/s41556-018-0138-8.

78. Lee, J., Li, M., Milwid, J., Dunham, J., Vinegoni, C., Gorbatov, R., Iwamoto, Y., Wang, F., Shen, K., Hatfield, K., et al. (2012). Implantable microenvironments to attract hematopoietic stem/cancer cells. Proc. Natl. Acad. Sci. USA *109*, 19638–19643. https://doi.org/10.1073/pnas.1208384109.

79. Kyjacova, L., Saup, R., Rönsch, K., Wallbaum, S., Dukowic-Schulze, S., Foss, A., Scherer, S.D., Rothley, M., Neeb, A., Grau, N., et al. (2021). IER2-induced senescence drives melanoma invasion through osteopontin. Oncogene *40*, 6494–6512. https://doi.org/10.1038/s41388-021-02027-6.

80. Dobin, A., Davis, C.A., Schlesinger, F., Drenkow, J., Zaleski, C., Jha, S., Batut, P., Chaisson, M., and Gingeras, T.R. (2013). STAR: ultrafast universal RNA-seq aligner. Bioinformatics *29*, 15–21. https://doi.org/10.1093/bioinformatics/bts635.

Please cite this article in press as: Elbanna et al., Environmentally induced cell stiffening shapes metastatic site selection by tuning the immune vulnerability of cancer cells, Immunity (2026), https://doi.org/10.1016/j.immuni.2026.06.025

STAR★METHODS

KEY RESOURCES TABLE

REAGENT or RESOURCE	SOURCE	IDENTIFIER
Antibodies		
Anti-GAPDH antibody	Cell Signaling	Cat#2118L; RRID: AB_561053
IRDye 680RD Goat anti-Rabbit IgG Secondary Antibody	Li-Cor Biosciences	Cat#926-68071
IRDye 800CW Goat anti-Mouse IgG Secondary Antibody	Li-Cor Biosciences	Cat#926-32210
APC conjugated anti-CD8a antibody	Tonbo Biosciences	Cat#20-0081; RRID: AB_2621150
eFluor660 conjugated anti-Lamp1 antibody	eBiosciences	Clone: 1D4B; Cat#50-1071-82
PE conjugated anti-TNF	BioLegend	Cat#506306; RRID: AB_315427
PE/Cy7 conjugated anti-IFNγ	BioLegend	Cat#505826; RRID: AB_2295770
PerCP-Cy5.5 conjugated anti-NK1.1 antibody	eBioscience	Cat# 45-5941-82
InVivoMab anti-mouse CD8α	Bio X Cell	Cat# BE0004-1; Clone: 53–6.7; RRID: AB_1107671
Anti-Asialo GM1	Wako Chemicals	Cat# 986-10001; RRID: AB_516844
InVivoPlus rat IgG2a isotype control	Bio X Cell	Cat# BP0089; Clone: 2A3; RRID: AB_2894744
InVivoPlus mouse IgG2b isotype control	Bio X Cell	Cat# BP0086; Clone: MPC-11; RRID: AB_2894741
Anti-CD8 rabbit monoclonal	Cell Signaling Technology	Cat# 98941; RRID: AB_2756376
Anti-NKp46 goat polyclonal	R&D Systems	Cat# AF2225; RRID: AB_355192
Percp-cy5.5 CD45 mouse	BioLegend	Cat# 103130; Clone: 30-F11; RRID: AB_893339
CD45 human	eBioscience	Clone HI30, cat# 11-0459-42
Mouse osteopontin	R&D Systems	Cat# AF808; RRID: AB_2194992
human CD3	Leica	Cat# NCL-L-CD3-565, clone LN10; RRID: AB_563541
human CD8	DAKO	Cat# M7103, clone C8/144B
human CD45	DAKO	Cat# M0701, clone 2B11
human CD56	Marque	Cat# 156R-96, clone MRQ42
MHCII AF700	eBioscience	Cat# 56-5321-80
Cd11b PE-FIRE	Biolegened	Cat#101279
Ly6C BV711	Biolegend	Cat#128037; RRID: AB_2562630
CCR2 BV650	Biolegend	Cat#150613; Clone: SA203G11; RRID: AB_2721553
F4/80 APC-Cy7	Biolegend	Cat#123117; RRID: AB_893489
CD80 FITC	eBioscience	Cat#11-0801-82
CD86 BV605	Biolegend	Cat#105037, clone: GL-1; RRID: AB_11204429
Cd11c PE-Cy7	eBioscience	Cat#25-0114-82
human fc block	BD Biosciences	Clone Fc1; cat #564219; RRID: AB_2728082
CTV	Invitrogen	cat#C34557
anti-EPCAM-eFluor660	Invitrogen	Clone 1B7, cat#50-9326-42
Biological samples		
Human metastatic spine samples	Department of Neurosurgery MSKCC	N/A

(*Continued on next page*)

Please cite this article in press as: Elbanna et al., Environmentally induced cell stiffening shapes metastatic site selection by tuning the immune vulnerability of cancer cells, Immunity (2026), https://doi.org/10.1016/j.immuni.2026.06.025

Continued

REAGENT or RESOURCE	SOURCE	IDENTIFIER
Chemicals, peptides, and recombinant proteins		
Dapi	Thermo Fisher Scientific	Cat#D1306
PI	Invitrogen	Cat#P3566
D-Luciferin, potassium salt	Goldbio	Cat#LUCK-1G
Fibronectin, Bovine Plasma	Millipore Sigma	Cat#341631-5MG
Alexa Fluor 647 Phalloidin	Invitrogen	Cat#A22287
IL-2	Proleukin, Prometheus	Cat#65483011607
NK Cell Isolation Kit, mouse	Miltenyi Biotec MACS	Cat#130-115-818
BD Cytofix/Cytoperm Plus Kit (with BD GolgiPlug)	BD	Cat#555028
RNeasy Mini Kit	QIAGEN	Cat#74106
Luna One Step qPCR	NEB	Cat#E3005L
4% PFA	Electron Microscopy Sciences	Cat#30525-89-4
Collagenase IV	Gibco	Cat#17104019
Dnase	Sigma-Aldrich	Cat#69182-3
trametinib	Selleck Chemicals	Cat#871700-17-3
palbociclib	Selleck Chemicals	Cat#827022-32-2
Brefeldin A	Sigma-Aldrich	Cat#20350-15-6
RIPA buffer	Sigma-Aldrich	Cat#20-188
R-OPN	R&D Systems	Cat#441-OP
Opn Elisa kit	Invitrogen	Cat#EMSPP1
Opn primer pair	OriGene	Cat#MP215080
mouse interferon gamma	BioLegend	Cat#575304
Deposited data		
WT vs PRF scRNA seq data	GEO	GEO: GSE331042
Published Melanoma scRNA seq data (Pozniak et al.)	EGA	EGA: EGAD00001009291
Bulk RNA seq	GEO	GEO: GSE330079
Spatial Transcriptomics	GEO	GEO: GSE329415
TCGA PanCancer Atlas Cohort	Hoadley et al.[76]	N/A
Experimental models: Cell lines		
B16F10	Massagué Lab	N/A
YUMM5.2	Boire Lab	N/A
MC38	Ganesh Lab	N/A
Experimental models: Organisms/strains		
Mouse:C57BL/6J	The Jackson Laboratory	Strain#000664
Mouse:OT1:B6.129S6-Rag2tm1Fwa Tg(TcraTcrb)1100Mjb	Taconic Farms	Strain#2334
Mouse: CByJ.B6-Prf1tm1Sdz/J	The Jackson Laboratory	Strain#007079
Mouse: B6(Cg)-Tyrc-2J/J	The Jackson Laboratory	Strain#000058
Mouse:C57BL/6J	The Jackson Laboratory	Strain#000664
Software and algorithms		
Living Image software v.2.50	Perkin – Elmer	N/A
FlowJo software v10.7.1	BD	N/A
Imaris software v8	Bitplane	N/A
CaseViewer	3D Histech	N/A
Prism v8	GraphPad	N/A
R Studio + R	Posit PBC	N/A
Xenium Explorer	10x	N/A

(*Continued on next page*)

Please cite this article in press as: Elbanna et al., Environmentally induced cell stiffening shapes metastatic site selection by tuning the immune vulnerability of cancer cells, Immunity (2026), https://doi.org/10.1016/j.immuni.2026.06.025

Continued

REAGENT or RESOURCE	SOURCE	IDENTIFIER
Custom code for spatial transcriptomics	Github	https://github.com/ElbannaYassmin/Spatial-Transcriptomics-of-bone-tissue-PRF1−−B16F10-injected-mice-vs-healthy-controls.git
Custom code for scRNA-seq	Github	https://github.com/ElbannaYassmin/Single-Cell-RNA-sequencing-analysis-of-WT-vs-PRF1−−B16F10-injected-mice
Custom code for bulk RNA-seq	Github	https://soccin.github.io/pwg-docs/methods/rnaSeq.html

EXPERIMENTAL MODEL AND SUBJECT PARTICIPANT DETAILS

Mice

The animal protocols used in this study were approved by the Institutional Animal Care and Use Committee of Memorial Sloan Kettering Cancer Center. Metastasis experiments employed healthy, 6–8 week old male mice of the following genotypes: C57BL/6J (Strain #00064), B6(Cg)-*Tyr*$^{c-2J}$/J (B6 Albino, Strain #00058)), or CByJ.B6-Prf1tm1Sdz/J (Strain #007079) (*Prf1*$^{-/-}$), purchased from the Jackson Laboratory. Males were used as recipients in these studies to minimize sex-based immune responses against male B16F10 cells. Mice were assigned randomly into groups for all *in vivo* experiments. Healthy, 2-6 month old OT-1 αβTCR transgenic mice and C57BL/6J mice of both sexes (obtained from Jackson Laboratory) were used to generate OT-1 CTLs and NK cells, respectively, for *in vitro* assays. All animals were housed under specific pathogen free conditions.

Human studies

Spinal metastases containing both epidural and osseous components were collected from breast cancer patients and NSCLC patients indicated for surgery. Breast cancer patients were female, 65 and 48 years old at time of surgery. NSCLC patients were male, and female, ages 50 and 64, respectively, at time of surgery. Human tissues were obtained under Memorial Sloan Kettering Cancer Center (MSKCC) Institutional Review Board-approved protocol 17-593, titled "Defining the Immunological Tumor Microenvironment on Metastatic and Primary Spine Tumors." Clinical information was abstracted from medical records and de-identified. Informed consent was obtained from all patients.

Cell lines

B16F10 cells (male) were cultured at 37 °C in RPMI supplemented with 10% FBS, 1 mM sodium pyruvate, 2 mM L-glutamine, 50 U/mL penicillin, and 50 μg/mL streptomycin. MC38 (female) and YUMM5.2 cells (male) were cultured at 37 °C in DMEM medium with 10% FBS, 2 mM GlutaMAX, 50 U/mL penicillin, and 50 μg/mL streptomycin. HEK293T cells (used to generate ecotropic lentivirus) were cultured at 37 °C in DMEM supplemented with 10% FBS, 1 mM sodium pyruvate, 2 mM L-glutamine, 50 U/mL penicillin, and 50 μg/mL streptomycin. All cell lines were negative for mycoplasma and viral pathogens.

METHOD DETAILS

Cytotoxic lymphocyte preparation

To generate OT-1 CTLs, splenocytes from OT-1 αβTCR transgenic mice were mixed with congenic splenocytes pulsed with 100 nM OVA and cultured in RPMI medium with 10% FBS and 0.55 mM β-mercaptoethanol. After 24 hours, cells were supplemented with 30 IU/mL IL-2 (NIH BRB Repository) and split as needed. Functional assays were performed after 7 days in culture. Murine NK cells were isolated from C57BL/6J splenocytes using negative selection (NK cell isolation kit, MACS, 130-115-818) and incubated overnight with 1000 U/mL IL-2.

CRISPR-Cas9 targeting

B16F10 cells were genetically modified to generate *Spp1*$^{-/-}$ and *Rosa26*-targeted lines using CRISPR-Cas9. Guide RNAs (gRNAs) targeting the *Spp1* and *Rosa26* loci were designed and synthesized by Synthego. Cells were transfected with multiguide gRNAs and Cas9 using Lipofectamine, followed by clonal expansion. Successful knockouts were confirmed by Sanger sequencing to validate genomic edits and by immunoblot to assess protein loss. Recombinant osteopontin (R&D Systems) was used to rescue phenotypic effects in *Spp1*$^{-/-}$ cells. In these experiments, cells were treated with osteopontin protein at 1 μg/mL for 24 hours before functional assays.

Metastasis assays

Unless otherwise stated, 4×10^5 cancer cells were injected into the tail vein of 6–8 week old C57BL/6J mice, and 2×10^5 cancer cells into the tail vein of 6–8 week old *Prf1*$^{-/-}$ mice, both in 200 μL of PBS. For intracardiac injections, 2.5×10^5 cells (YUMM5.2 or MC38)

Please cite this article in press as: Elbanna et al., Environmentally induced cell stiffening shapes metastatic site selection by tuning the immune vulnerability of cancer cells, Immunity (2026), https://doi.org/10.1016/j.immuni.2026.06.025

were injected in 100 μL PBS into the left cardiac ventricle. Mouse hair was removed using clippers to prevent interference with bioluminescent imaging (BLI). Metastatic burden in the lungs and femurs was quantified weekly following retro-orbital injection of D-luciferin (150 mg/kg) and imaging using the IVIS Spectrum Xenogen instrument (Caliper Life Sciences) equipped with Living Image software v.2.50. For NK depletion experiments, 4×10^5 (IgG control) or 2×10^5 (NK depletion) B16F10 cells were injected into the tail vein of 6–8 week old B6(Cg)-Tyrc-2J/J mice (Jackson Labs, 000058). NK cell depletion was performed by intraperitoneal (i.p.) injection of anti-asialo GM1 antibody (Wako Chemicals, 986–10001), as previously described,[77] 6 days and 1 day before tail vein injection of cancer cells and once weekly thereafter. $CD8^+$ T cell depletion was achieved by administering 250 μg of InVivoMab anti-mouse CD8α antibody (clone 53-6.7, BioXCell, BE0004-1) or IgG2a control (BioXCell, BE0089) by i.p. injection 2 days and 1 day before tumor delivery, followed by weekly injections, as previously described.[29] Survival and paralysis-free survival (defined as the time until bilateral hind leg paralysis) were tracked for all mice. Mice were euthanized upon reaching the endpoint criteria of paralysis, metastatic burden in the lungs, or other signs of significant distress.

Killing, degranulation, and cytokine production assays

For CTL functional assays, cancer cell targets were cultured overnight on fibronectin-coated 96-well plates in the presence of 20 ng/mL IFNγ (to enhance class I MHC expression), loaded with varying concentrations of OVA for 2 hours, and washed three times with medium. To assess killing, OT-1 CTLs were added at a 4:1 effector-to-target (E:T) ratio, and the lysis of target cells (GFP^+CD8^-) was tracked using the Incucyte S3 (Sartorius). PI (Thermo Fisher Scientific) was used to mark dead cells, and images were taken every hour for 8 hours to capture the kinetics of cell death. To assess lytic granule secretion, CTLs were mixed with B16F10 targets at a 2:1 E:T ratio and incubated for 90 minutes at 37 °C in the presence of eFluor660-conjugated anti-Lamp1 antibody (1 μg/mL, Clone 1D4B, eBiosciences). Cells were stained with anti-CD8a antibody, and the percentage of $Lamp1^+$ CTLs ($CD8^+$) was quantified by flow cytometry. For cytokine production, CTLs were added at a 2:1 E:T ratio and incubated for 4 hours at 37 °C in the presence of BD GolgiPlug protein transport inhibitor (BD Biosciences). Cells were then stained with anti-CD8a, fixed, permeabilized using the BD Cytofix/Cytoperm kit, and labeled with PE-conjugated anti-TNF (BioLegend, 506306) and PE/Cy7-conjugated anti-IFNγ (BioLegend, 505826) antibodies. The percentage of cytokine-producing CTLs ($CD8^+$) was quantified by flow cytometry. For NK cell functional assays, cancer cell targets were cultured overnight on fibronectin-coated 96-well plates, mixed with NK cells at a 4:1 ratio, and target cell lysis was measured using the Incucyte S3. PI flux was employed to quantify cell death, with images taken every hour for 8 hours to track real-time killing. For assays using hydrogel substrates, hydrogel arrays (Matrigen) were coated with 10 μg/mL fibronectin (Millipore Sigma) in PBS at 37°C for 2 hours to allow sufficient protein coating. Following incubation, excess fibronectin was aspirated, and the wells were washed once with PBS to remove any unbound fibronectin. B16F10 cells were then plated at a density of 30,000 cells per well in complete growth medium and incubated at 37°C overnight. Subsequent cocultures were performed as described above.

In vitro cell growth and proliferation assays

To assess proliferation, B16F10 cells were labeled with CellTrace Violet (CTV, Thermo Fisher) as per the manufacturer's protocol, and CTV dilution was measured daily by flow cytometry.

Histology

Murine lung and bone tissue was perfused and fixed overnight at 4°C with 4% PFA. Fixed bone was then decalcified in 10% EDTA (pH 7.4) at 4 °C for 2-3 weeks with periodic monitoring to ensure complete decalcification. The tissues were then dehydrated through a graded ethanol series, cleared in xylene, and embedded in paraffin. 5 μm sections were stained for NKp46 (R&D Systems, Cat # AF2225) and CD8 (Cell Signaling Technology, Cat # 98941). Immunohistochemical staining of human tissue samples was performed on the Leica Bond RX automated platform. Heat-induced epitope retrieval (HIER) was conducted using ER2 buffer (Leica, Cat# AR9590) at 97 °C for 30 minutes, followed by primary antibody incubation for 30 minutes at room temperature using antibodies against CD3 (Leica, Cat # NCL-L-CD3-565), CD8 (DAKO, Cat # M7103), CD45 (DAKO, Cat # M0701), or CD56 (Marque, Cat # 156R-96). Detection was performed using the Leica Bond Polymer Refine Detection DAB Kit (Cat# DS9800). All slide imaging was carried out using a Pannoramic Scanner fitted with a 20×/0.8NA objective (3D Histech), and the results visualized using CaseViewer software (3D Histech).

Atomic Force Microscopy (AFM) Data Collection

Cells were seeded on glass-bottom Petri dishes (FluoroDish FD5040) coated with fibronectin and maintained in complete RPMI medium supplemented with 10 mM HEPES pH 7.0 during the acquisition of stiffness maps. Experiments were conducted at 37 °C using an MFP-3D-BIO AFM microscope (Oxford Instruments) with cantilevers fitted with 5 μm diameter colloidal borosilicate probes (nominal spring constant k = 0.1 N/m, Novascan). The exact spring constant of the cantilever was determined before each experiment using the thermal noise method, and its optical sensitivity was calibrated using a PBS-filled glass-bottom Petri dish as an infinitely stiff surface. Each session involved testing 10-12 cells from each experimental group. Bright field images of each cell were captured during AFM measurements using an inverted optical objective (Zeiss AxioObserver Z1) integrated with the AFM system. Stiffness maps of 60 μm × 60 μm (18 × 18 points) were acquired in areas containing both cells and substrate at a rate of 1.5 Hz for a single approach/withdrawal cycle. A trigger point of 1 nN was set to ensure a penetration depth of 1-2 μm.

Suspended Microchannel Resonator (SMR) Data Collection

Single-cell size-normalized acoustic scattering (SNACS) was measured using a previously described SMR-based method.[32] Before each set of measurements, the SMR was treated with 0.25% Trypsin-EDTA for 30 minutes, followed by a 3-minute wash with 10% bleach and a final 5-minute rinse with DI-H_2O. After cleaning, the SMR was passivated with 1 mg/mL poly(L-lysine)-graft-poly(ethylene glycol) (PLL-g-PEG) in H_2O for 10 minutes at room temperature, followed by a 5-minute rinse with PBS + 2% FBS (FACS buffer). All measurements were performed at room temperature in FACS buffer. The SMR was briefly rinsed with the same buffer between each experiment. During measurements, cells were loaded into the SMR through 0.005-inch inner diameter fluorinated ethylene propylene (FEP) tubing. Fluid flow across the SMR was controlled using three independent electronic pressure regulators (MPV1, Proportion Air) and three solenoid valves (S070, SMC). A consistent differential pressure was applied across the SMR to maintain constant shear forces and data acquisition rate during cell measurement. All regulators, valves and data acquisition systems were operated by custom software developed in LabVIEW 2017 (National Instruments). The vibration frequency of the SMR cantilever was continuously monitored during measurements.

Immunofluorescence imaging

B16F10 cells were fixed in 2% PFA, washed in PBS, and then labeled with Alexa Fluor 647-labeled phalloidin (1:400, Invitrogen) and DAPI (1:1000, Sigma). To quantify F-actin intensity, phalloidin images was subjected to intensity thresholding in Imaris (Bitplane) to establish the space occupied by cells, after which the average intensity of phalloidin within the cellular volume was determined.

Hydrogel Scaffold Fabrication

Hydrogel scaffolds were fabricated following previously reported methods.[78] Soda lime glass beads were sorted using an Advantech Sonic Sifter to ensure a consistent size range, with ~8% deviation. The beads were dispersed in deionized water and gradually loaded into an 8 × 35 mm glass vial to a height of 2–2.5 mm. They were then mechanically packed into a lattice structure using an ultrasonic water bath. Preparations were then dried in a 60°C oven and thermally annealed for 4 hours in a furnace at temperatures between 650°C and 680°C, depending on the bead size. A hydrogel precursor solution was prepared immediately before use, consisting of 15% (soft) or 30% (stiff) acrylamide monomer, 1.5 wt% bis-acrylamide crosslinker, 0.2 vol% N,N,N′,N′-tetramethylethylenediamine accelerator, and 0.2 vol% 2-hydroxy-2-methylpropiophenone photoinitiator in nitrogen-purged deionized water. The precursor solution (150 μL) was infiltrated into the glass bead template and centrifuged at 4,000 × g for 15 minutes. It was then polymerized under a 15 W ultraviolet light source for 15 minutes. The polyacrylamide hydrogel–glass templates were removed from the glass vials the following day to ensure complete polymerization. Any excess hydrogel was removed by scraping the glass bead template with a razor blade on all surfaces. Glass beads were selectively dissolved in alternating washes of an acid solution: a 1:5 dilution of hydrofluoric acid in 1.2 M hydrochloric acid and 2.4 M hydrochloric acid. The washes were performed on a shake plate, with solutions being changed every 4 hours until the beads were fully dissolved. Scaffolds were thoroughly washed with deionized water to remove any residual acid and then lyophilized. After lyophilization, the scaffolds were resuspended in Cryomatrix embedding resin and cut to a thickness of 1 mm using a CryoStar NX70. Following further washing in deionized water, the scaffolds were sterilized with 70% ethanol and stored at 4°C in sterile phosphate-buffered saline (PBS) solution. The final pore dimension of the optimized scaffolds used in the study was 300 ± 16 μm.

Subcutaneous Hydrogel Implantation

Mice were anesthetized using 1.5% isoflurane, and their dorsal fur was removed with electric clippers followed by Nair hair removal cream. The skin was sterilized using 70% isopropyl alcohol prep wipes and povidone-iodine to minimize the risk of infection. Prior to the surgical procedure, each mouse received a subcutaneous injection of meloxicam (2 mg/kg) for analgesia. Two small horizontal incisions (2 mm) were made in the left and right flanks of the mouse. A subcutaneous pocket was carefully created at each incision by inserting surgical scissors and gently expanding them. Each pocket was then implanted with a single hydrogel scaffold. One scaffold was composed of 15% polyacrylamide, and the other scaffold was composed of 30% polyacrylamide, allowing for a direct comparison between the two materials within the same animal. The incisions were closed using two Reflex 7-mm wound clips, ensuring secure closure and promoting optimal healing. Postoperative care included daily meloxicam treatment for 3 days to provide continuous pain relief. The wound clips were removed after 7 days to allow for full tissue recovery.

Mouse Tissue Collection and Processing

All plasticware used in the procedure was precoated with 0.05% BSA, and centrifuges were pre-cooled to 4°C. Lungs and knees were digested in 1 mL of digestion buffer (2 mL Collagenase I [7.5 mg/mL], 1.49 mg DNase I, 8 mL 1% BSA in HBSS++) per mouse. For lung tissue, tumors were resected and digested in 10 mL of digestion buffer for 20 minutes at 37°C with rotation. After digestion, the material was strained, washed with 5 mL of SMEM + 2% FBS, and resuspended in 1 mL of SMEM + 2% FBS. Red blood cells were lysed with 10 mL of 1× RBC Lysis for 1 minute, followed by neutralization with 10 mL of SMEM + 2% FBS, at which point the sample was strained again. Cells were Fc-blocked (1:200) (Clone 2.4G2, cat #70-0161) for 10 minutes at 4°C, followed by staining with anti-CD45-PerCPCy5 (1:200) (Clone 30-F11, cat #103132) and DAPI. Finally, cells were resuspended in 1 mL of PBS + 2% FBS for sorting. For knee tissue, the bones were cleaned, crushed in 1 mL of digestion buffer, and transferred to precoated Eppendorf tubes. An additional 1 mL of digestion buffer was added, and the samples were incubated at 37 °C for 30 minutes, with gentle

pipetting every 10 minutes to facilitate digestion. Cells were processed following the same procedure as the lung samples. Both lung and knee tissue samples were subjected to FACS on a BD FACSAria to isolate GFP$^+$CD45$^-$DAPI$^-$ cancer cells.

Human Tumor Tissue Processing

Tumors isolated from the spine were digested in 5 mL of digestion buffer (2 mL Collagenase I [7.5 mg/mL], 1.49 mg DNase I, 8 mL 1% BSA in HBSS++) for 20 minutes at 37°C with rotation. After digestion, the material was strained, washed with 5 mL of SMEM + 2% FBS, and resuspended in 1 mL of SMEM + 2% FBS. Red blood cells were lysed with 10 mL of 1× Pharm Lysis for 1 minute, followed by neutralization with 10 mL of SMEM + 2% FBS, at which point the sample was strained again. Cells were Fc-blocked (1:200) (Clone Fc1, cat #564219) for 10 minutes at 4°C, then stained with anti-CD45-FITC (1:200) (Clone HI30, cat#11-0459-42) and anti-EPCAM-eFluor660 (1:200) (Clone 1B7, cat#50-9326-42), followed by DAPI staining. Cells were then resuspended in 1 mL of 2% FBS in PBS for sorting, which was carried out on a BD FACSAria to isolate EPCAM$^+$CD45$^-$DAPI$^-$ cells.

Single Cell RNA Sequencing Library Preparation

GFP$^+$CD45$^-$ B16F10 MTCs were FACS-purified from wild type lung, *Prf1*$^{-/-}$ lung, and *Prf1*$^{-/-}$ bone, then hashed using oligonucleotide-conjugated antibodies (TotalSeq B, hashes 1, 2, and 3) to uniquely label individual samples. The cells were then pooled together in equal proportions to enable multiplexed scRNA-seq. Single-cell gel bead-in-emulsions (GEMs) were generated using the 10x Genomics Chromium platform. Reverse transcription and cDNA amplification were performed according to the 10x Genomics 3' v3 protocol. Separate libraries were generated for the gene expression and hashing data. Libraries were sequenced on an Illumina platform to achieve a minimum of 50,000 reads per cell for gene expression and 5,000 reads per cell for hashing.

Xenium Slide Preparation

Sections for Xenium were prepared according to the Xenium In Situ for FFPE – Tissue Preparation Guide (CG000578 Rev D; 10x Genomics) protocol. For spatial transcriptomics, a series of 5 μm-thick longitudinal sections were cut across the femur, floated in an RNase-free water bath, then carefully mounted within the probe field of Xenium slides containing the Prime 5K Mouse panel with custom add-ons (Table S2).

Demineralized Bone Paper (DBP) Colony Formation Assay

Bovine femurs were sourced locally, cleaned, and cut into cortical bone blocks, then lipid-extracted with 1:1 chloroform:methanol. Decalcification was enhanced by exposing femur segments to 1.2 N HCl under hydrostatic pressure, with solutions replaced daily for 5-7 days. Post-demineralization, bone segments were cryosectioned into 20 μm sheets of demineralized bone paper (DBP). Transmission imaging confirmed preserved lamellar collagen structures. Murine osteogenic cells were isolated from eGFP mice, with femur and tibia marrow removed by centrifugation. Bones were chopped (~1–2 mm), enzymatically digested in α-MEM with 10% FBS, 1% P/S, and collagenase (800 U), then rinsed three times with PBS and cultured in α-MEM. After five days, osteoprogenitor cells migrating from bone fragments were harvested and expanded on tissue culture plastic. Cells at passages 3–5 were used for experiments. For differentiation, 10^4 osteoprogenitors were seeded onto DBP and cultured in osteogenic medium with 10 mM β-glycerophosphate and 200 μM L-ascorbic acid. Osteoblasts (10^4) were seeded onto DBP in 96-well plates and cultured in osteogenic medium for seven days to induce remineralization. RFP-labeled melanoma cells (control and *Spp1*$^{-/-}$) were added at 25 cells/well in α-MEM with 10% FBS and P/S. Cocultures were imaged every two days over 12 days using a fluorescent microscope (EVOS). Melanoma cell area, colony number, and colony size were quantified with ImageJ.

Enzyme-linked immunosorbent assay (ELISA)

To assess osteopontin secretion in relation to environmental stiffness, B16F10 cells were cultured on hydrogel substrates of differential stiffness, and culture supernatants were collected after 24 hours. Osteopontin levels were measured with the mouse Osteopontin Elisa Kit (Invitrogen, EMSPP1) using the manufacturer's recommended protocol.

Quantitative real-time PCR

Total RNA was isolated from cell samples using the Qiagen RNeasy Plus Mini Kit according to the manufacturer's standard protocol. RNA concentrations were quantified with a NanoDrop spectrophotometer. For cDNA synthesis, 2 μg of RNA was reverse transcribed using the Luna One-Step RT-PCR Kit (New England Biolabs) according to the manufacturer's instructions. Relative gene expression levels were quantified using *Gapdh* as the housekeeping gene for normalization.

Immunoblots

B16F10 cells were cultured for 7 days in 25 nmol/mL trametinib and 500 nmol/mL palbociclib (both from Selleckchem) to induce senescence, which has been reported to enhance osteopontin expression.[79] To trap osteopontin in intracellular compartments, certain samples were treated with 1 μg/mL Brefeldin A at 37°C for 8 hours prior to harvest. Cells were lysed in RIPA buffer containing protease inhibitors (cOmplete mini cocktail, EDTA-free, Roche) and the soluble fractions subjected to SDS-PAGE, followed by transfer to nitrocellulose. Osteopontin was detected using a polyclonal antibody (R&D Systems AF808), with Gapdh (Cell Signaling Technology, clone D16H11) as a loading control.

Please cite this article in press as: Elbanna et al., Environmentally induced cell stiffening shapes metastatic site selection by tuning the immune vulnerability of cancer cells, Immunity (2026), https://doi.org/10.1016/j.immuni.2026.06.025

QUANTIFICATION AND STATISTICAL ANALYSIS

Statistics

Analyses were carried out using either representative experiments or pooled data as indicated (*n* is defined in the figure legends for each experiment). Statistical tests (two-tailed Mann-Whitney, two-tailed ANOVA, paired and unpaired two-tailed t-tests and Log-rank Mantel-Cox tests) were performed using GraphPad Prism. Unless otherwise indicated, error bars denote SEM. No statistical methods were used to determine sample size prior to experiments.

scRNA-seq analysis

B16F10 MTCs

Raw sequencing data were demultiplexed and aligned to the mouse reference genome using Cell Ranger (v6.1.2) from 10x Genomics, which was then used to generate gene expression matrices and hashtag oligonucleotide (HTO) counts for downstream analysis. Cell hashing data were demultiplexed using the Seurat (v4.3.0) HTODemux function to assign sample identity to individual cells. The data were filtered based on mitochondrial content (>10%), unique feature counts, and total RNA counts to remove potential doublets and dead cells, followed by normalization and scaling using the SCTransform function in Seurat. Principal component analysis (PCA) was carried out, followed by UMAP projection for dimensionality reduction. Clustering was performed using the Louvain algorithm, and clusters were annotated based on canonical marker gene expression. Differential gene expression analysis was conducted between samples using the FindMarkers function in Seurat with the Wilcoxon rank-sum test. Genes with an adjusted p-value < 0.05 were considered statistically significant. Reanalysis of patient melanoma: scRNA-seq data were obtained from a cohort of pre-treatment melanoma patients after post-filtering of low-quality cells and annotation of malignant cells using inferCNV.[44] Normalization and scaling were performed using Seurat (v4.3), and gene expression data were log-normalized using Seurat's NormalizeData() function. To assess cytoskeletal regulation, gene lists were compiled from KEGG and GSEA sources (Table S4). Module scores were calculated using Seurat's AddModuleScore() function across the full dataset as well as a subset of pre-treatment cells. These scores were used to evaluate pathway-level expression in relation to immune infiltration. Module score distributions were visualized using violin plots. Statistical significance between groups was assessed using Wilcoxon rank-sum tests unless otherwise stated.

Spatial Transcriptomic Analysis

Spatial transcriptomics data was generated using the 10x Genomics Xenium platform with a 5K panel containing custom add-ons (Table S2). Analyses were performed in R (v4.4.3) with Seurat (v5.3.0) and SeuratObject (v5.2.0) on Red Hat Linux 8.6. Molecule filtering was applied using a QV threshold of 20 to create the cell-gene expression matrix. Six datasets (2 tumor and 1 healthy control mouse, duplicate samples) were merged into a single Seurat object with sample-specific cell IDs. Cells with fewer than 10 transcripts were excluded to remove low-quality cells and extreme outliers. Filtered data was normalized with SCTransform, selecting 3,000 variable genes. PCA was performed on normalized data, followed by graph-based clustering (resolution 0.07). Clusters were manually annotated using marker gene expression, spatial, and histological context, guided by canonical markers, transcriptional profiles, and H&E images. Differential gene expression analysis further enabled identification of *Spp1*-high melanoma cells. To characterize the local cellular microenvironment around melanoma cells, we conducted a spatial neighborhood analysis using cell centroid coordinates from Xenium segmentation. Cell-type annotations were combined with 2D centroid positions to define neighborhoods. For a selected population (e.g. *Spp1*-high melanoma), the nine nearest neighbors were identified via a k-nearest neighbors (KNN) approach, excluding self-neighbors. Neighbor identities were recorded and aggregated across query cells, then normalized to proportions to create neighborhood profiles. Analyses were done separately for *Spp1*-high melanoma and *Spp1*-low melanoma cells for direct comparison. Permutation testing assessed whether certain cell types were enriched or depleted beyond chance by shuffling labels 1,000 times while keeping positions and structure. Null distributions were generated for each cell type, and enrichment ratios and p-values were calculated. Low-abundance or biologically irrelevant cell types were excluded from visualization. The same approach was applied to osteolineage cells to evaluate spatial colocalization.

Bulk RNA-seq analysis

FASTQ files were generated from bulk RNA sequencing and mapped to the UCSC mm10 mouse genome (GTF: Mus_musculus.GRCm38.80) using STAR (v2.5.0a).[80] The two-pass alignment method was used, where reads were first aligned using known annotated junctions from Ensembl. Novel junctions identified in the first pass were included in the second pass, during which the RemoveNoncanonical flag was applied. Aligned reads were post-processed with PICARD (v1.124) to add read groups and convert SAM files to sorted, compressed BAM files. Gene expression quantification was performed using HTSeq (v0.5.3) with default parameters. Raw count matrices generated by HTSeq were normalized and analyzed for differential expression using DESeq (R/Bioconductor, v3.2.0). Differential gene expression was assessed using DESeq, applying the Wald test and correcting for multiple testing using the Benjamini-Hochberg method. Genes with an adjusted p-value < 0.05 were considered significant. Normalized log2 expression values were used to perform hierarchical clustering with the Pearson correlation distance metric. Additional dimensionality reduction was performed using multidimensional scaling (MDS) and principal component analysis (PCA). Heatmaps were generated using the heatmap.2 function from the gplots R package, displaying the top 100 differentially expressed genes with

mean-centered, normalized log2 expression values. Gene set enrichment analysis (GSEA) was conducted using gene sets from the Broad MSigDB. For groups with fewer than three samples, GSEAPreranked was applied using log2 fold changes generated by DESeq.

Analysis of clinical data

The TCGA PanCancer Atlas Study was accessed through the cBioPortal (https://www.cbioportal.org/). The gene *Spp1* was queried and copy number alteration (CNA) profiles were examined using the ''Cancer Types Summary'' view. This analysis was used to assess the distribution of *Spp1* copy number gains (amplifications) and losses (deletions) across cancer types. The relative frequencies of amplifications and deletions were compared across tumor types to evaluate cancer type-specific patterns of *Spp1* genomic alteration within the TCGA PanCancer Atlas cohort.[76]

SMR analysis

Cell-induced SMR frequency shifts were used to quantify the node deviation (ND), which reflects acoustic scattering of individual cells, and the buoyant mass (BM) of the cells. ND is size-dependent, so it must be normalized to enable comparison across cells of varying volumes. We applied a normalization method as described in ref[32]. To determine cell volume (V), we first we first measured the average cell volume ($\overline{V}$) using a Coulter Counter (Beckman Coulter). Individual cell volumes were then inferred using the relationship:

$$V = \frac{BM}{\overline{BM}}\,\overline{V}$$

where $\overline{BM}$ is the mean buoyant mass, estimated by fitting the distribution of buoyant mass measurements to a log-normal function. We then computed the size-normalized acoustic scattering (SNACS) value for each cell using the equation:

$$SNACS = NV - m(V_{ref} - V)$$

Here, $NV = ND/V$ is the volume-normalized node deviation, and m is the slope obtained from a linear regression of NV versus V across the population. The reference volume V_{ref} was defined as the median cell volume.

AFM analysis

Force curves for each map were fitted using the Hertz model (Igor Pro, Wavemetrics). Data fitting was performed within the first 1 μm of indentation, specifically in the range of 0 to 50% of the maximum applied force. The following settings were used for the fitting: tip Poisson's ratio ν_tip = 0.19, tip Young's modulus E_tip = 68 GPa, and sample Poisson's ratio ν_sample = 0.45. Stiffness histograms were obtained by identifying the stiffness values associated with each individual cell (excluding the substrate values). Data from each sample were pooled as a single population. Measurements made < 500 nm above the substrate were excluded from the analysis.